Optimal Patterns and Control for Sampling via Mobile Sensor Networks

Dmitrijs Gurkins

A Thesis

Presented to the Faculty

of Princeton University

in Candidacy for the Degree

of Master of Science in Engineering

Recommended for Acceptance

by the Department of

Mechanical and Aerospace Engineering

June 2007

Abstract

This thesis concerns optimal patterns and control for sampling using a network of mobile sensors. In the current work we are strongly motivated by coordinated adaptive control of Autonomous Underwater Vehicles (AUV's) for ocean sampling. With some adaptations, however, this work could apply to other sensor platforms.

The core value of the work presented in this thesis is in providing guidelines on how to use multiple vehicles for collecting the data. The goal is to use available resources in the best possible way, i.e. collect the richest data set. We make assumptions about the available resources and quantitatively define the notion of 'richness' of a data set in terms of a metric.

To derive such a metric, we review the methods of Objective Analysis (OA), a powerful data assimilation scheme that is commonly used in evaluating the performance of a sampling experiment. In its usual form, however, the OA method is impractical for metric-driven optimization of the sampling tracks due to the significant computation time. We then present a recent result by Francois Lekien and colleagues which allows us to compute the OA metric much faster.

The OA metric is then used to find patterns on a simple domain that would have optimal performance for various experiments. We focus our attention on structured sampling patterns – parameterizable and repeatable elliptical tracks – and compare their performance to the 'lawn mower patterns' that are traditionally used for sampling. We present the results of pattern optimization in terms of dimensionless parameters which allows us to apply those results to a range of sampling experiments in the ocean as well as in the air.

After establishing the guidelines for pattern design, we consider the control laws necessary to stabilize the gliders to those patterns. Some of the control laws that apply to the patterns presented here were already published by Derek Paley, Rodolphe Sepulchre and Naomi Leonard. The focus of the work presented here is extending those results to resonance patterns. Finally, we simulate the vehicle motion with resonance control and demonstrate the convergence to a desired configuration.

Acknowledgements

First and foremost I would like to thank my advisor, Professor Naomi Ehrich Leonard for her guidance, encouragement and support throughout my graduate career at Princeton. I am very fortunate and honored to be able to work with her. Every graduate student must be dreaming to have an advisor like Naomi. I thank her for the freedom she gave me in choosing the focus of my research and her wisdom in helping me narrow the scope of my work. She has been an inspiring role model for me from the day I met her during my visit as a prospective student in the summer of 2004. In fact, meeting Naomi and experiencing her enthusiasm was a deciding factor for coming to Princeton.

I express my sincere thanks to the reader of this thesis, Professor Anand Gnanadesikan. I highly appreciate his comments and guidance, which has greatly helped improve the quality of my thesis and increased my knowledge of the subject. Coming from an engineering and math background and working on such an interdisciplinary research topic, it was great to have Anand as a mentor. His deep knowledge of oceanography and vast experience in the field has helped me find the right balance between theory and application of the current work.

I cannot thank enough Francois Lekien who was always in the office next door (even late at night), available to share his expertise and help me out with whatever I needed. He was there when I could not figure out a problem for Math class; he was there when I needed help with the research; and he was always there when I simply needed someone to talk to.

Derek Paley has been a great mentor and a great friend since the day we met. Always busy, yet always willing to help me with everything from LaTeX code to details of sophisticated control laws. He has a great talent as a teacher and I wish him all the best in his career as a professor.

I also thank the other students in the Dynamical Control Systems Laboratory and the faculty, students and post-docs in my department, whose comments and discussions have helped my research. Thanks also to all of the administrators and staff members in the MAE department who have helped me during my time here. Special thanks to Jessica O'Leary for always being 'on top of it'.

Most of all, I thank my family for their love, support, advice and encouragement. I also thank my girlfriend Satomi and all of my great friends from Princeton for their company, encouragement and friendship.

This thesis carries the number T-3171 in the records of the Department of Mechanical and Aerospace Engineering.

Contents

Chapter 1

Introduction

The coverage problem refers in general to the measure of quality of service of a sensor network. It has a variety of applications including telecommunication, sampling, distribution and wireless networks [15]. In this thesis we focus our attention on the problem of *sampling* an area using a network of mobile sensors in order to collect the best possible data set using the resources available. One can apply these results to other applications of coverage theory (satellite or wireless connectivity for example), but to be concrete, we frame the development in this thesis with a specific application in mind: using mobile sensor network to optimally cover a region and collect data for an oceanographic experiment.

1.1 The Power of Coordination

There are many applications where *coordinated* motion of multiple vehicles or systems is desirable. The applications range from automated highway systems to coordinated adaptive control of Autonomous Underwater Vehicles (AUV's). There is a trend in the military towards autonomous air and underwater vehicles, where teams of unmanned vehicles are tasked to perform 'dirty', 'dull', and

'dangerous' operations, such as border patrol and maritime search and rescue [7], as well as robotic exploration of other planets [28]. One of the peaceful applications of coordinated motion, Robo Cup, is a competition open to robotic soccer teams, which is drawing the attention of researchers from all over the world [10].

With recent technological developments, coordinated control of vehicles has gained a lot of interest in the oceanographic community [35]. A single vehicle could be insufficient for large-scale experiments such as AOSN-II or ASAP described in Section 1.3.2, and several vehicles (i.e a sensor network) might be more suitable to collect high-resolution data over large domains. Consider for example the task of re-constructing a field of temperature distribution in a part of the ocean. Using a fleet of AUV's as a mobile sensor network allows us to collect temperature measurements at different spatial and temporal points within the domain. However, if the vehicles are not coordinated, it is possible that they will all bunch up in one spot and collect redundant measurements or separate so far apart that it would be impossible to interpolate the data between the measurement sites. Either case poses severe limitations to our ability to reconstruct the field in the given domain. A solution to this problem is achieved through a *coordinated motion of the vehicles*, such that the entire network is designed to maximize the usefulness[1] of the data. Coordinated periodic trajectories such as the ones studied in this thesis, provide means to collect measurements with desired spatial and temporal separation.

[1]We will define the notion of 'usefulness' in Chapter 3 using the theoretical development and a metric described in Chapter 2

1.2 Historic Perspective on Coordinated Motion

The problems of collective motion and collective stabilization have been of interest to researchers for a very long time. The classic anecdote of great Dutch physicist Christiaan Huygens dating back to 1665 marks the beginning of scientific inquiry about such problems. Christiaan Huygens was the inventor of a pendulum clock and on one day in February 1665 was confined to his bed by a minor illness [38]. He stared at two clocks he had built, which were hanging side by side. He noticed something odd: the two pendulums were swinging in perfect synchrony. He tried disturbing them, but only after a short time, they regained synchrony. Huygens postulated that the two clocks were somehow influencing each other, perhaps through tiny air movements or imperceptible vibrations of their common support. Sure enough, when he moved them to the opposite sides of the room, the clock gradually fell out of step. It turned out that Huygens's observation initiated an entire subbranch of mathematics: the theory of coupled oscillators [38]. It is important to note that the framework of coupled oscillators can be applied to a large family of problems seemingly unrelated to the Huygens's clock. Many physical and biological phenomena can be modeled with great accuracy using those simple oscillators that retain the essence of their biological prototypes. Coupled oscillators can be found throughout the natural world: pace maker cells in the heart and neural networks in the brain and spinal cord that control such behaviors as breathing, running and chewing. Crickets chirping in unison and giant congregations of fireflies all flashing synchronously are examples of oscillators not confined to a single organism. Remarkably, the behavior of *fish schools* which motivated research in sensor networks and their coordinated motion can be modeled using the same principles. The direction of

each fish can be thought of as an oscillator, so the entire school moving in one direction is an example of collection of coupled oscillators in synchrony [27].

1.2.1 Kuramoto Model

Collective synchronization was first studied mathematically by Wiener ([41] and [42]), who recognized its ubiquity in the natural world. Unfortunately Wiener's mathematical approach based on Fourier integrals [41] has turned out to be a dead end [39]. A more fruitful approach was pioneered by Winfree [43] in his first paper where he formulated the problem in terms of a huge population of interacting limit-cycle oscillators. Winfree exploited a separation of timescales: on a short timescale, the oscillators relax to their limit cycles, and so can be characterized solely by their phases; on a long timescale, these phases evolve because of the interplay of weak coupling and slight frequency differences among the oscillators. In a further simplification, Winfree supposed that each oscillator was coupled to the collective rhythm generated by the whole population [39].

Inspired by Winfree's discoveries, a Japanese scientist Yoshiki Kuramoto began working on collective synchronization in 1975. His first paper on the topic [16] was a brief note announcing some exact results about what would come to be known as *The Kuramoto Model*. The Kuramoto model consists of a population of N coupled phase oscillators $\theta_k(t)$ having natural frequencies ω_k distributed with a given probability density $g(\omega)$, and whose dynamics are governed by

$$\dot{\theta_k} = \omega_k + \sum_{j=1}^{N} K_{kj} \sin(\theta_j - \theta_k), \quad k = 1, \ldots, N, \tag{1.1}$$

where K_{kj} are positive scalars. Thus each oscillator tries to run independently at its own frequency, while the coupling tends to synchronize it to all the others.

By making a suitable choice of rotating frame, $\theta_k \to \theta_k - \Omega t$ in which Ω is the first moment of $g(\omega)$, Eq. (1.1) transforms to an equivalent system of phase oscillators whose natural frequencies have zero mean. When the coupling is sufficiently weak, the oscillators run incoherently, whereas beyond a certain threshold collective synchronization emerges spontaneously [39].

To visualize the dynamics of the phases, it is convenient to imagine a swarm of points running around the unit circle in the complex plane. The complex order parameter

$$re^{i\psi} = \frac{1}{N}\sum_{j=1}^{N} e^{i\theta_j} \tag{1.2}$$

is a macroscopic quantity that can be interpreted as the collective rhythm produced by the whole population [20]. It corresponds to the centroid of the phases. The radius $r(t)$ measures the phase coherence, and $\psi(t)$ is the average phase (see Figure 1.1).

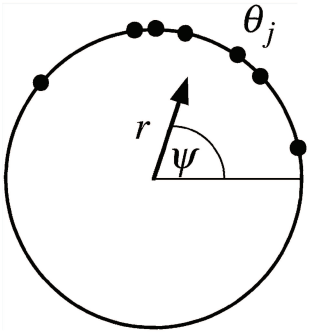

Figure 1.1: Geometric interpretation of the order parameter (1.2). The phases θ_j are plotted on the unit circle. Their centroid is given by the complex number $re^{i\psi}$, shown as an arrow. Reprinted from [39].

For instance, if all the oscillators move in a single tight clump, then $r \approx 1$ and the population acts like a giant oscillator. On the other hand, if the oscillators are scattered around the circle, then $r \approx 0$; the individual oscillations act incoherently and no macroscopic rhythm is produced. Defining K as a

coupling strength common to all oscillators, we rewrite Equation 1.1 as

$$\dot{\theta_k} = \omega_k + \frac{K}{N}\sum_{j=1}^{N}\sin(\theta_j - \theta_k). \tag{1.3}$$

Kuramoto noticed that the governing equation (1.3) can be rewritten neatly in terms of the order parameter. Multiply both sides of the order parameter equation (1.2) by $e^{-i\theta_k}$ to obtain

$$re^{i(\psi-\theta_k)} = \frac{1}{N}\sum_{j=1}^{N}e^{i(\theta_j-\theta_k)}.$$

Equating imaginary parts yields

$$r\sin(\psi - \theta_k) = \frac{1}{N}\sum_{j=1}^{N}\sin(\theta_j - \theta_k).$$

Thus (1.1) becomes

$$\dot{\theta_k} = \omega_k + Kr\sin(\psi - \theta_k), \quad k = 1, \ldots, N. \tag{1.4}$$

Much of the future work in coupled phase oscillators theory and coordination *including the approach taken in this thesis* is motivated by Kuramoto's simple model.

1.3 Current Trends in Ocean Sampling

With recent technological developments, it has became possible to extend the traditional methods of collecting the data in the ocean such as via sensors located on buoys and drifters (quasi-static sensors) and mobile sensors located on ships, to *autonomous vehicles* equipped with sensors and capable of navi-

gating in the ocean for extended periods of time. Not only are such vehicles less expensive to operate, but also they provide rich data sets in the areas often unreachable by other means such as underneath ice shelves in Antarctica [6]. Autonomous vehicles can be used in formation, creating a *Mobile Sensor Network* where each vehicle is controlled in a way that is optimal for the performance of the entire network.

Historically, oceanographic sampling has either tended to be done with low numbers of steerable platforms (ships), or large numbers of nonsteerable platforms (floats). In case of the steerable platforms, the goal is to cover as much of the domain with as short a track as possible. For experiments involving a fleet of drifting floats, oceanographers usually space them out as much as possible and hope for the best. The advent of steerable gliders means that alternative strategies may be preferable, and this study represents an early step in evaluating such strategies. With those new technologies at hand, the basic question is formulated as: *what is the best way to deploy mobile sensors to measure a field that is evolving in space and time, and how do to get the sensors to organize themselves to optimally sample such a field?*

1.3.1 Gliders

A strong motivation for our work is the emergence of Autonomous Underwater Vehicles (AUV's) as important observation platforms for oceanographic exploration. One of the types of AUV's, often referred to as 'gliders' due to their design, relies on buoyancy regulation using a ballast tank and internal mass distribution for motion control. Gliders do not use thrusters or propellers and have limited external moving control surfaces, which makes them ideal for long-term missions due to their energy efficiency. The gliders use fixed wings to provide

lift which induces motion in the horizontal direction. The nominal motion of a glider in the longitudinal plane is along a saw-tooth trajectory. While propeller-driven vehicles operate on the order of hours, the gliders are designed to operate autonomously for several weeks. Their design allows them to remotely upload the collected data via satellite link and receive new waypoints without the need for human input.

The gliders have on-board 'low-level' controls that allow them to travel to the waypoints specified by the 'high-level' control. The waypoints can be determined centrally for all gliders based on the data from navigational sensors onboard gliders as well as environmental data such as temperature, salinity and flow fields. In this thesis our focus is on the *high-level control* of the gliders. The low-level controls are assumed to be ideal in the sense that the gliders do whatever they need to follow prescribed waypoints in the absence of disturbances. With this assumption, the low-level controls are ignored in further analysis. The reader is referred to [35] for additional information about the gliders and technical details.

From the fluid mechanics point of view, the motion of an underwater vehicle is determined by its shape, size, total mass, and distribution of mass as well as properties of surrounding fluid and disturbances. In this thesis, however, we are concerned with a high-level picture of the problem and ignore the individual dynamics of gliders focussing on the *dynamics of a formation* of multiple gliders, regarding each of them as a *point-mass particle*.

1.3.2 Sea Trials

Two major sea trials in Monterey Bay, CA provided a test bed for control algorithms and a real-world demonstration of capabilities of coordinated sensor

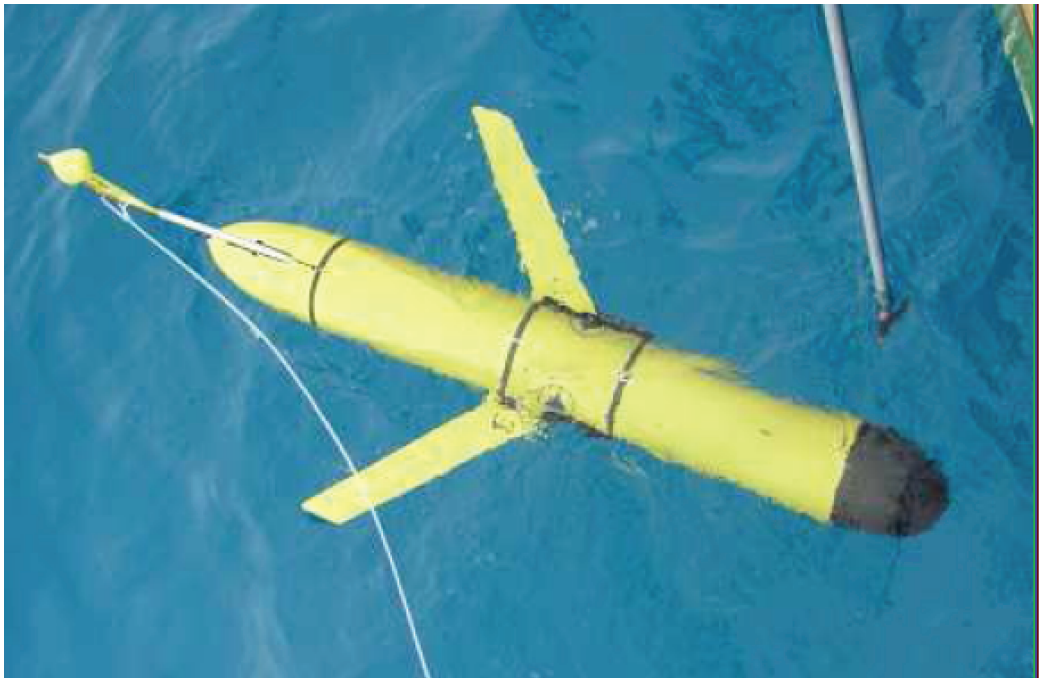

Figure 1.2: Slocum glider used in Monterey Bay experiments.

networks. The Autonomous Ocean Sampling Network II (AOSN-II) project was aimed at developing a sustainable, integrated observation-modeling system for oceans [34]. Among the wide range of objectives of this collaborative project were developing components of adaptive sampling infrastructure, designing adaptive sampling methods intended to provide optimal data to ocean models and improving understanding of ocean science through data collected by various platforms. During the AOSN-II field experiment in August 2003, oceanographic data from satellites, surface drifters, ships, airplanes, propeller-driven vehicles and buoyancy-driven gliders were assimilated into predictive ocean models. Two types of AUVs, Spray and Slocum, played a crucial role in the experiment collecting vast amounts of data in the given domain that extended as far as 100 kilometers from shore deeper than 400 meters.

Another large-scale experiment in Monterey Bay was carried out in August 2006 as part of the Adaptive Sampling and Prediction (ASAP) project [1].

Building upon the frameworks of AOSN-II, researchers in the ASAP 2006 experiment introduced a completely automated (no human in the loop) control system for gliders and collected an invaluable data set for understanding dynamic processes in the ocean.

In the AOSN-II field experiment gliders traversed preplanned sampling paths. The paths were 80-100 km lines perpendicular to the shore for the Spray gliders whereas for the Slocum gliders the tracks were polygons. The shape of the glider tracks were chosen based on experience of the collaborating oceanographers taking into account spatial and temporal scales of interest and physical limitations of the sensor array and the gliders. In the ASAP field experiment both Spray and Slocum gliders were controlled to and coordinated on superelliptic tracks that were adapted over the course of the month-long experiment. A metric to quantify the richness of the data set was used to help select these tracks and patterns [23]. This thesis presents a numerical optimization study that provides some further guidelines on choosing useful sampling patterns for certain kinds of data-collecting experiments.

1.4 Thesis Overview

Optimal sampling via mobile sensor network involves (1) establishing a metric for performance evaluation that can be computed quickly, (2) applying this in an oceanographically relevant context, and (3) figuring out how to get the network of gliders to organize themselves for optimal performance. The chapters of this thesis follow this basic outline.

In Chapter 2 we review the methods of Objective Analysis (OA), a powerful data assimilation scheme originally developed by Eliassen et al [12] in 1954 and later independently reproduced and popularized by Gandin [13] in 1963. Al-

though commonly used in evaluating the performance of a sampling experiment [35], the method may be impractical for metric-driven optimization of the sampling tracks due to the significant computation time. A new theoretical result due to Francois Lekien and colleagues [21] and presented in Section 2.2 allows much faster OA metric evaluation.

The OA metric described in Chapter 2 is used in Chapter 3 as a measure of richness of data collected on a given sampling trajectory. We focus our attention on *structured sampling patterns* - parameterizable and repeatable elliptical tracks. To validate our approach we also consider in Section 3.3 the 'lawn mower patterns' that were traditionally used for sampling ([2] and [14]) and quantitatively compare their performance to performance of the structured patterns. We implement a modified steepest ascent algorithm to find patterns that produce the richest data set (largest value of the OA metric) as a function of dimensionless oceanographic parameters $S_{\mathfrak{z}}$ and $S\mathfrak{t}$ representing size of the domain and duration of the experiment with respect to spatial and temporal decorrelation scales respectively. Noticing certain trends in the resulting patterns, we limit the parameter set to channel the computational resources to finding the best patterns as a function of region in $(S_{\mathfrak{z}}, S\mathfrak{t})$ space. The results of pattern optimization are presented in Figure 3.9 and the corresponding subsets of parameter space $(S_{\mathfrak{z}}, S\mathfrak{t})$ are identified in Figure 3.10.

In Chapter 4 we review the control laws presented in [36] and [31], and extended those results in Section 4.3 to *the resonance patterns*. Resonance patterns include a set of closed curves such that the perimeter of each curve is an integer multiple of some distance d. This approach allows the vehicle to move along tracks of different size, yet still be 'synchronized'. We follow a framework described in detail in [18] and [23] where the control input u_k is the rate of change of heading of each vehicle. It is an assumption that the vehicles move

with uniform speed. Finally, we simulate the vehicle motion with resonance control in Section 4.3.2 and demonstrate in Figure 4.1 the convergence to a desired relative phase configuration.

We conclude with Chapter 5 where we give an overview of the results, identify contributions to the field of sampling via mobile sensor networks, and point out some of the limitations of the work presented in this thesis. Also in Chapter 5 we provide some directions for future research pertinent to the material covered in this work.

Chapter 2

Objective Analysis

In this chapter, we review the classical Objective Analysis (OA) method in the context of evaluating the performance of sampling paths for mobile sensor platforms (e.g. gliders and propeller-driven AUV's) in a specified domain. OA is a data assimilation and estimation scheme. OA mapping error provides a measure of uncertainty in the sampling scheme and can be used to evaluate sampling performance (the reader is referred to [5] and [13] for fundamentals of OA methods). When designing optimal sampling trajectories or sampling plans, the metric must be computed for each candidate trajectory. As a consequence, such optimization problems rely on the ability to compute the metric as fast as possible. It turns out that computing the metric using the classical Objective Analysis methods is a computationally costly procedure, making it impractical for real-time metric-driven optimization of sampling trajectories. Here we derive analytical results that allow us to compute the metric in a fraction of the time it would normally take following classical OA schemes. The work presented here is due to Francois Lekien and collaborators, and some of the derivations appear in [21].

Objective Analysis is also commonly referred to as Optimal Interpolation. It was originally developed by Eliassen et al [12] in 1954 and independently reproduced and popularized by Gandin [13] in 1963. An extensive study of this assimilation scheme and its application to ocean science can be found in [3], [5] and [19]. The goal of Objective Analysis in ocean modeling is to reconstruct the continuous field of a particular measured quantity. For example a temperature field in Monterey Bay CA is a continuous field sampled by discrete measurements of the fleet of underwater gliders. Incorporating measurements from all gliders and all times on a grid allows us to approximate the temperature distribution in that area. The more *distributed* measurements we have the more certain we are that our approximation reflects reality. Note that the case when lots of measurements are taken in the same place does not provide a good coverage of the sampling domain. OA mapping error gives a useful measure of richness of the data set by taking into account not just the quantity of measurements but how they are distributed in space and time with respect to the dominant spatial and temporal scales in the sampled field.

2.1 The Classic Discretized OA

In this section, we derive the classical formulation of Objective Analysis following [21]. We also show, based on the OA error map (or equivalently OA certainty map), how to compute the metric that we use to quantify the performance of the array.

We view the real system state as a random vector $\rho_{bg} \in \mathbb{R}^N$. Each component of ρ_{bg} represents, for example, the temperature at one of the grid points. We define N as the number of grid points, which are simply points in space (3D in general) and in time where the field is to be recreated. Next we define

$\hat{\rho} = E[\rho_{bg}]$ which is assumed known. We also assume that we have an estimate on the covariance of that vector:

$$\mathbf{B} = E[(\rho_{bg} - \hat{\rho})(\rho_{bg} - \hat{\rho})^\top]. \tag{2.1}$$

Each row i of $\mathbf{B}$ corresponds to a grid point (x_i, t_i) and each column j corresponds to grid point (x_j, t_j), where x_i is the location (in 3D in general) in space and t_i is the time of the ith grid point. The element B_{ij} is the *covariance* between these two points. The diagonal elements are variances and represent the a priori estimated error at a grid point. The goal of OA is to get M measurements and use them to get a better estimate ρ_a that minimizes the covariance matrix $\mathbf{A}$:

$$\mathbf{A} = E[(\rho_a - \hat{\rho})(\rho_a - \hat{\rho})^\top]. \tag{2.2}$$

The diagonal elements of $\mathbf{A}$ are variances and represent the a posteriori error at a grid point. Each measurement is made at a point y_k and at a time t_k and results in a measured value T_k of the field. Since the OA works on a regular grid, chances are that the measurements are not made exactly on a grid point. For this purpose, we compute a *measurement matrix* $\mathbf{H} \in \mathbb{R}^{M \times N}$, which represents both the position and time of the measurements. For example, one might interpolate the data using the closest point on the mesh. This means that for any measurement at y_k and time t_k, we expect to measure the same value as $\hat{\rho}$ at the closest grid point. In this case, $\mathbf{H}$ contains only M non-zero elements and each is in a different row. For each measurement, we put a '1' in the row of $\mathbf{H}$ corresponding to this measurement and the column corresponding to the closest grid point.

We expect the vector T containing M measurements $T = (T_1, \ldots, T_M)^\top$ to be

$$T = \mathbf{H}\hat{\rho} + \epsilon, \tag{2.3}$$

where ϵ is a measurement error. Here, following [25] we assume that $E[\epsilon] = 0$, i.e. the measurements are unbiased.

OA is characterized by how it creates the new state ρ_a based on the background state ρ_{bg} and the new measurements. We present the following hypotheses:

1. The new state ρ_a is unbiased: $E[\rho_a] = \hat{\rho}$.

2. ρ_a is given by the background state plus a *linear* increment, $T - \mathbf{H}\rho_{bg}$, which represents the data 'mismatch'. In other words, we require that

$$\rho_a = \rho_{bg} + \mathbf{Q}(T - \mathbf{H}\rho_{bg}) \tag{2.4}$$

   for some $\mathbf{Q} \in \mathbb{R}^{N \times M}$.

3. Following [21], the norm of $\mathbf{A}$ is defined as[1]

$$||\mathbf{A}||_1 = \frac{1}{\dim(\mathbf{A})}\mathrm{Tr}(\mathbf{A}). \tag{2.5}$$

   where $\dim(\mathbf{A})$ is the dimension of the matrix $\mathbf{A}$

[1] Technically, it does not matter whether we have $1/\dim(\mathbf{A})$ or not since it is a constant. Once we have a norm, we can always multiply it by a constant and we get an equivalent norm. Furthermore, the original references such as [13] do not have it. So why include it? Two reasons:
1) If we do not divide $\mathrm{Tr}(\mathbf{A})$ by $\dim(\mathbf{A})$, the value of the norm increases with the resolution. That is, suppose that we have a mesh with 100 points, then $\mathrm{Tr}(\mathbf{A})$ is roughly 100 times the average error. With a 1000 grid points, the norm is 10 times what we had with coarse resolution. If we divide by the dimension, we get a similar number for any resolution.
2) When we do the continuous case, we compute the integral of $\mathbf{A}$ over the domain (as if we had an infinite number of points in the discrete case). So, one way to view the continuous case is as the limit of the discrete case when the number of (regularly spaced) grid points is going to infinity. But clearly that would not work if we do not divide by $\dim(\mathbf{A})$.

4. The resulting covariance matrix $\mathbf{A}$ is "minimum". This determines the matrix $\mathbf{Q}$ introduced above. It is not possible to minimize all elements of $\mathbf{A}$ at the same time, so we minimize the norm of $\mathbf{A}$ as defined in Eq. (2.5) to obtain $\mathbf{Q}$:

$$\min_{\mathbf{Q}\in\mathbb{R}^{N\times M}}\{||\mathbf{A}||_1\}. \tag{2.6}$$

Rewriting Eq. (2.4) as

$$\rho_a - \hat{\rho} = \rho_{bg} - \hat{\rho} + \mathbf{Q}\left(\underbrace{T - \mathbf{H}\hat{\rho}}_{\epsilon} - \mathbf{H}(\rho_{bg} - \hat{\rho})\right), \tag{2.7}$$

we manipulate Eq. (2.2) as following:

$$\begin{aligned}
\mathbf{A} &= E[(\rho_a - \hat{\rho})(\rho_a - \hat{\rho})^\top] \\
&= \underbrace{E[(\rho_{bg} - \hat{\rho})(\rho_{bg} - \hat{\rho})^\top]}_{=\mathbf{B}} + \mathbf{Q}\underbrace{E[\epsilon\epsilon^\top]}_{=\mathbf{W}}\mathbf{Q}^\top \\
&\quad + \mathbf{Q}\mathbf{H}\underbrace{E[(\rho_{bg} - \hat{\rho})(\rho_{bg} - \hat{\rho})^\top]}_{=\mathbf{B}}\mathbf{H}^\top\mathbf{Q}^\top \\
&\quad + \underbrace{E[(\rho_{bg} - \hat{\rho})\epsilon^\top]}_{=0}\mathbf{Q}^\top - \underbrace{E[(\rho_{bg} - \hat{\rho})(\rho_{bg} - \hat{\rho})^\top]}_{=\mathbf{B}}\mathbf{H}^\top\mathbf{Q}^\top \\
&\quad + \mathbf{Q}\underbrace{E[\epsilon(\rho_{bg} - \hat{\rho})^\top]}_{=0} - \mathbf{Q}\underbrace{E[\epsilon(\rho_{bg} - \hat{\rho})^\top]}_{=0}\mathbf{H}^\top \\
&\quad \mathbf{Q}\mathbf{H}\underbrace{E[(\rho_{bg} - \hat{\rho})(\rho_{bg} - \hat{\rho})^\top]}_{=\mathbf{B}} - \mathbf{Q}\mathbf{H}\underbrace{E[(\rho_{bg} - \hat{\rho})\epsilon^\top]}_{=0}\mathbf{H}^\top\mathbf{Q}^\top \\
&= \mathbf{B} + \mathbf{Q}(\mathbf{W} + \mathbf{H}\mathbf{B}\mathbf{H}^\top)\mathbf{Q}^\top - \mathbf{B}\mathbf{H}^\top\mathbf{Q}^\top - \mathbf{Q}\mathbf{H}\mathbf{B}.
\end{aligned} \tag{2.8}$$

Let $\hat{\mathbf{Q}}$ be the optimal solution that minimizes $\mathbf{A}$ and define

$$\mathbf{Q} = \hat{\mathbf{Q}} + \delta\mathbf{Q}.$$

The corresponding variation on $\mathbf{A}$ is

$$\delta\mathbf{A} = \mathbf{A}|_{\mathbf{Q}=\hat{\mathbf{Q}}+\delta\mathbf{Q}} - \mathbf{A}|_{\mathbf{Q}=\hat{\mathbf{Q}}}.$$

Hence, Eq. (2.8) becomes

$$\begin{aligned}\delta\mathbf{A} &= \delta\mathbf{Q}\left(\mathbf{W}+\mathbf{HBH}^\top\right)\hat{\mathbf{Q}}^\top + \hat{\mathbf{Q}}\left(\mathbf{W}+\mathbf{HBH}^\top\right)\delta\mathbf{Q}^\top \\ &\quad -\delta\mathbf{QHB} - \mathbf{BH}^\top\delta\mathbf{Q}^\top. \end{aligned} \tag{2.9}$$

Using the norm in (2.5) and noting that $\delta\left(\mathrm{Tr}(\mathbf{A})\right) = \mathrm{Tr}(\delta\mathbf{A})$ we have

$$\delta\mathrm{Tr}(\mathbf{A}) = \mathrm{Tr}\left(\delta\mathbf{Q}(\mathbf{W}+\mathbf{HBH}^\top)\hat{\mathbf{Q}}^\top + \hat{\mathbf{Q}}(\mathbf{W}+\mathbf{HBH}^\top)\delta\mathbf{Q}^\top - \delta\mathbf{QHB} - \mathbf{BH}^\top\delta\mathbf{Q}^\top\right)$$

By using the fact that $\mathrm{Tr}(\cdot)$ is linear and $\mathrm{Tr}(\mathbf{X}) = \mathrm{Tr}(\mathbf{X}^\top)$, we get

$$\delta\mathrm{Tr}(\mathbf{A}) = 2\ \ \mathrm{Tr}\left(\left(\hat{\mathbf{Q}}(\mathbf{W}+\mathbf{HBH}^\top) - \mathbf{BH}^\top\right)\delta\mathbf{Q}^\top\right)$$

In order to get $\delta\mathrm{Tr}(\mathbf{A}) = 0$, the right side of the equation above must vanish for all $\delta\mathbf{Q}^\top$. Noting that $\mathrm{Tr}(\mathbf{X}\delta\mathbf{Q}^\top) = 0 \Longleftrightarrow \mathbf{X} = 0$, we must have

$$\hat{\mathbf{Q}}(\mathbf{W}+\mathbf{HBH}^\top) - \mathbf{BH}^\top = 0,$$

which is a linear equation in $\hat{\mathbf{Q}}$ and accepts one and only one solution:

$$\hat{\mathbf{Q}} = \mathbf{BH}^\top(\mathbf{W}+\mathbf{HBH}^\top)^{-1}. \tag{2.10}$$

To finish the derivation, we use the result above in Eq. (2.8) to get the usual form of OA:

$$\mathbf{A} = \mathbf{B} - \mathbf{B}\mathbf{H}^{\top}(\mathbf{W} + \mathbf{H}\mathbf{B}\mathbf{H}^{\top})^{-\mathbf{1}}\mathbf{B}. \tag{2.11}$$

The norm of $\mathbf{A}$ in (2.5) can be used as a metric to characterize sampling performance [13]. However, this approach proves to be too computationally intensive to perform any form of optimization with reasonable number of metric evaluations that could be completed within reasonable time. We now proceed to develop a continuous version of Objective Analysis scheme that allows us to compute the metric much more efficiently. The reader is referred to [23] for an overview of the OA and its application to oceanographic experiments. Additional theoretical background and examples of uses of OA can be found in [3] and [19].

2.2 Continuous Objective Analysis

This section presents work by Francois Lekien and colleagues that has appeared in [21]. Similar ideas were explored earlier in [25] and [24]. We assume that we are interested in a random field (e.g. temperature, salinity) that takes real values at each point x in space and each time t. We denote this field $\hat{T}(x,t)$ or more simply $\hat{T}(\mathbf{z})$ where we use the new vector $\mathbf{z}$ to concatenate space and time $\mathbf{z} = (x,t)$.

We introduce a *reconstructed function* $T_{obs}(\mathbf{z})$, which is the continuous quantity representing the 'current-time knowledge' of the field after a measurement is made. In practice, discrete measurements are taken and this field must be reconstructed. For example, $T_{obs}(\mathbf{z})$ can be the temperature observed by the

closest sensor to the point $\mathbf{z}$. The exact method how this function is reconstructed is irrelevant for this theoretical development.

Conceptually, the goal of the measurement process is to determine this reconstructed function $T_{obs}(\mathbf{z})$ such that we have

$$\omega(\mathbf{z})\left(\hat{T}(\mathbf{z}) + n(\mathbf{z}) - T_{obs}(\mathbf{z})\right) \approx 0 \quad \forall \mathbf{z}, \tag{2.12}$$

where $n(\mathbf{z})$ is an estimate on the sensor noise with $\mathbf{E}[n(\mathbf{z})] = 0$, and $\omega(\mathbf{z})$ is a weighting function. However, as we will see further, $T_{obs}(\mathbf{z})$ does not appear in the final equation that we use to calculate the metric, so we are not concerned *how* it is determined. With regards to the sensor noise, we also define $N(\mathbf{z}) = \mathbf{E}[n^2(\mathbf{z})]$ and assume that

$$\mathbf{E}[n(\mathbf{z})n(\mathbf{z}')] = N(\mathbf{z})\delta(\mathbf{z} - \mathbf{z}').$$

The function $\omega(\mathbf{z})$ represents the generalized position of the sensor in space and time, and for the purposes of this study is assumed to be a Gaussian centered at the most probable position of the sensor.

As in the Classical OA (Sec. 2.1), we use the notion of "data misfit," which in the continuous case becomes

$$T_{obs}(\mathbf{z}') - T_b(\mathbf{z}') \tag{2.13}$$

where T_b is the current estimate. We create a new state $T_a(\mathbf{z})$ by adding a linear increment of the "data misfit" to the current state T_b

$$T_a(\mathbf{z}) = T_b(\mathbf{z}) + \int d\mathbf{z}' \; \alpha(\mathbf{z}, \mathbf{z}')\omega(\mathbf{z}') \left(T_{obs}(\mathbf{z}') - T_b(\mathbf{z}')\right). \tag{2.14}$$

At this point coefficient $\alpha(\mathbf{z}, \mathbf{z}')$ is the unknown. To get an understanding of what it is, first note that values from any $\mathbf{z}'$ influence what we are doing at $\mathbf{z}$. That's why α has two parameter $\mathbf{z}$ and $\mathbf{z}'$. Suppose for example that the data misfit is $T_{obs}(\mathbf{z}') - T_b(\mathbf{z}') = 10$. Then we must add $10 \times \alpha(\mathbf{z}, \mathbf{z}')$ to $T_b(\mathbf{z})$. Of course we loop over $\mathbf{z}'$ to check all the points and get $T_b(\mathbf{z})$. That's why we have the integral in Eq (2.14). Clearly we expect $\alpha(\mathbf{z}, \mathbf{z})$ to be much larger than $\alpha(\mathbf{z}, \mathbf{z}' \neq \mathbf{z})$. That is, the misfit near point $\mathbf{z}$ is more likely to result in a correction to $T_b(\mathbf{z})$ than the misfit at a point $\mathbf{z}'$ far away from $\mathbf{z}$. So, α is really just the 'translation' of adding a linear increment to T_b. When we write Equation 2.14, we don't know $\alpha(\mathbf{z}, \mathbf{z}')$, but we compute the resulting error (for an arbitrary $\alpha(\mathbf{z}, \mathbf{z}')$), then we identify the $\alpha(\mathbf{z}, \mathbf{z}')$ that minimizes the resulting error. The solution is Eq (2.28).

Returning to Eq (2.14), we rewrite it as

$$\begin{aligned} T_a(\mathbf{z}) - \hat{T}(\mathbf{z}) = T_b(\mathbf{z}) - \hat{T}(\mathbf{z}) + \\ \int d\mathbf{z}' \; \alpha(\mathbf{z}, \mathbf{z}')\omega(\mathbf{z}') \left(n(\mathbf{z}') - \left[T_b(\mathbf{z}') - \hat{T}(\mathbf{z}') \right] \right). \end{aligned} \tag{2.15}$$

Taking the expected value and using the fact that $E\left[\left(T_b(\mathbf{z}) - \hat{T}(\mathbf{z}) \right) n(\mathbf{z}') \right] = 0$ we get

$$\begin{aligned} A(\mathbf{z_1}, \mathbf{z_2}) = \mathbf{E}\left[\left(T_a(\mathbf{z_1}) - \hat{T}(\mathbf{z_1}) \right) \left(T_a(\mathbf{z_2}) - \hat{T}(\mathbf{z_2}) \right) \right] = \\ \mathbf{E}\left[\left(T_b(\mathbf{z_1}) - \hat{T}(\mathbf{z_1}) \right) \left(T_b(\mathbf{z_2}) - \hat{T}(\mathbf{z_2}) \right) \right] \\ + \int d\mathbf{z}' \int d\mathbf{z}'' \; \alpha(\mathbf{z_1}, \mathbf{z}')\alpha(\mathbf{z_2}, \mathbf{z}')\omega(\mathbf{z}')\omega(\mathbf{z}'')\mathbf{E}\left[n(\mathbf{z}')n(\mathbf{z}'') \right] \\ + \int d\mathbf{z}' \int d\mathbf{z}'' \; \alpha(\mathbf{z_1}, \mathbf{z}')\alpha(\mathbf{z_2}, \mathbf{z}')\omega(\mathbf{z}')\omega(\mathbf{z}'') \\ \mathbf{E}\left[\left(T_b(\mathbf{z}') - \hat{T}(\mathbf{z}') \right) \left(T_b(\mathbf{z}'') - \hat{T}(\mathbf{z}'') \right) \right] \\ - \int d\mathbf{z}' \; \alpha(\mathbf{z_1}, \mathbf{z}')\omega(\mathbf{z}')\mathbf{E}\left[\left(T_b(\mathbf{z}') - \hat{T}(\mathbf{z}') \right) \left(T_b(\mathbf{z_2}) - \hat{T}(\mathbf{z_2}) \right) \right] \\ - \int d\mathbf{z}' \; \alpha(\mathbf{z_2}, \mathbf{z}')\omega(\mathbf{z}')\mathbf{E}\left[\left(T_b(\mathbf{z}') - \hat{T}(\mathbf{z}') \right) \left(T_b(\mathbf{z_1}) - \hat{T}(\mathbf{z_1}) \right) \right], \end{aligned} \tag{2.16}$$

where we introduced $A(\mathbf{z_1}, \mathbf{z_2})$, the estimated error of the new state T_a. From here we can represent A in a concise notation

$$\begin{aligned} A(\mathbf{z_1}, \mathbf{z_2}) &= B(\mathbf{z_1}, \mathbf{z_2}) \\ &+ \int d\mathbf{z}' \int d\mathbf{z}'' \; \alpha(\mathbf{z_1}, \mathbf{z}')\alpha(\mathbf{z_2}, \mathbf{z}'')\omega(\mathbf{z}')\omega(\mathbf{z}'') \left[N(\mathbf{z}')\delta(\mathbf{z}' - \mathbf{z}'') + B(\mathbf{z}', \mathbf{z}'')\right] \\ &- \int d\mathbf{z}'\omega(\mathbf{z}') \left[\alpha(\mathbf{z_1}, \mathbf{z}')B(\mathbf{z_2}, \mathbf{z}') + \alpha(\mathbf{z_2}, \mathbf{z}')B(\mathbf{z_1}, \mathbf{z}')\right], \end{aligned} \tag{2.17}$$

where $B(\mathbf{z_1}, \mathbf{z_2})$ is the best estimate on the covariance between two different points with the norm

$$||B|| = \sqrt{\int d\mathbf{z} \; B(\mathbf{z}, \mathbf{z})}. \tag{2.18}$$

Defining the norm of $A(\cdot, \cdot)$ as

$$||A|| = \sqrt{\int d\mathbf{z} \; A(\mathbf{z}, \mathbf{z})} \tag{2.19}$$

we have

$$\begin{aligned} \|A\|^2 &= \|B\|^2 \\ &+ \int d\mathbf{z} \int d\mathbf{z}' \int d\mathbf{z}'' \alpha(\mathbf{z}, \mathbf{z}')\alpha(\mathbf{z}, \mathbf{z}'')\omega(\mathbf{z}')\omega(\mathbf{z}'') \left[N(\mathbf{z}')\delta(\mathbf{z}' - \mathbf{z}'') + B(\mathbf{z}', \mathbf{z}'')\right] \\ &- 2 \int d\mathbf{z} \int d\mathbf{z}' \omega(\mathbf{z}')\alpha(\mathbf{z}, \mathbf{z}')B(\mathbf{z}, \mathbf{z}') \end{aligned} \tag{2.20}$$

Therefore, in parallel with the steps in Section (2.1) we have

$$\begin{aligned} \delta \|A\|^2 &= -2 \int d\mathbf{z} \int d\mathbf{z}' \delta\alpha(\mathbf{z}, \mathbf{z}')\omega(\mathbf{z}')B(\mathbf{z}, \mathbf{z}') \\ &+ \int d\mathbf{z} \int d\mathbf{z}' \int d\mathbf{z}'' \left[\alpha(\mathbf{z}, \mathbf{z}')\delta\alpha(\mathbf{z}, \mathbf{z}'') + \alpha(\mathbf{z}, \mathbf{z}'')\delta\alpha(\mathbf{z}, \mathbf{z}')\right] \omega(\mathbf{z}')\omega(\mathbf{z}'') \times \\ &\qquad \left[N(\mathbf{z}')\delta(\mathbf{z}' - \mathbf{z}'') + B(\mathbf{z}', \mathbf{z}'')\right] \end{aligned} \tag{2.21}$$

or by substituting $\mathbf{z}'$ for $\mathbf{z}''$ in the first part of the second line

$$\begin{aligned}\delta\|A\|^2 = 2\int d\mathbf{z}\int d\mathbf{z}'\int d\mathbf{z}''\delta\alpha(\mathbf{z},\mathbf{z}')\omega(\mathbf{z}') \\ \times\left[\alpha(\mathbf{z},\mathbf{z}'')\omega(\mathbf{z}'')\left[N(\mathbf{z}')\delta(\mathbf{z}'-\mathbf{z}'')+B(\mathbf{z}',\mathbf{z}'')\right]-\delta(\mathbf{z}'-\mathbf{z}'')B(\mathbf{z},\mathbf{z}')\right]\end{aligned} \tag{2.22}$$

The equation above is satisfied for any arbitrary distribution $\delta\alpha(\mathbf{z},\mathbf{z}')$ if and only if we have $\forall\mathbf{z},\mathbf{z}'$:

$$\int d\mathbf{z}''\omega(\mathbf{z}')\left[\alpha(\mathbf{z},\mathbf{z}'')\omega(\mathbf{z}'')\left[N(\mathbf{z}')\delta(\mathbf{z}'-\mathbf{z}'')+B(\mathbf{z}',\mathbf{z}'')\right]-\delta(\mathbf{z}'-\mathbf{z}'')B(\mathbf{z},\mathbf{z}')\right]=0 \tag{2.23}$$

or the linear equation

$$\int d\mathbf{z}''\alpha(\mathbf{z},\mathbf{z}'')\omega(\mathbf{z}')\omega(\mathbf{z}'')\left[N(\mathbf{z}')\delta(\mathbf{z}'-\mathbf{z}'')+B(\mathbf{z}',\mathbf{z}'')\right]=\omega(\mathbf{z}')B(\mathbf{z},\mathbf{z}') \tag{2.24}$$

which we rewrite concisely as

$$\int d\mathbf{z}''\alpha(\mathbf{z},\mathbf{z}'')\Psi(\mathbf{z}',\mathbf{z}'')=\omega(\mathbf{z}')B(\mathbf{z},\mathbf{z}')\ , \tag{2.25}$$

where

$$\Psi(\mathbf{z}',\mathbf{z}'')=\omega(\mathbf{z}')\omega(\mathbf{z}'')\left[N(\mathbf{z}')\delta(\mathbf{z}'-\mathbf{z}'')+B(\mathbf{z}',\mathbf{z}'')\right]. \tag{2.26}$$

We define the *inverse* of Ψ as following:

$$\int d\mathbf{z}''\Psi^{-1}(\mathbf{z}'',\mathbf{z})\Psi(\mathbf{z}',\mathbf{z}'')=\delta(\mathbf{z}-\mathbf{z}'). \tag{2.27}$$

Having defined Ψ^{-1}, we can write the solution α of Eq. (2.24) as

$$\alpha(\mathbf{z},\mathbf{z}'')=\int d\mathbf{z}'''\,\omega(\mathbf{z}''')B(\mathbf{z},\mathbf{z}''')\Psi^{-1}(\mathbf{z}'',\mathbf{z}''') \tag{2.28}$$

and we substitute α in Eq. (2.17) to get

$$\begin{aligned} A(\mathbf{z}_1, \mathbf{z}_2) &= B(\mathbf{z}_1, \mathbf{z}_2) \\ &\quad - \int d\mathbf{z}' \int d\mathbf{z}'' \omega(\mathbf{z}') \omega(\mathbf{z}'') B(\mathbf{z}_1, \mathbf{z}'') \Psi^{-1}(\mathbf{z}', \mathbf{z}'') B(\mathbf{z}', \mathbf{z}_2). \end{aligned} \tag{2.29}$$

We can further simplify the equations by making the assumption that measurements are comparable to the true value of the field at the *exact* place and time of the measurements. In this case, we have

$$\omega(\mathbf{z}) = \sum_i \delta(\mathbf{z} - \mathbf{z}_i^m)$$

where the summation is made over the $i = 1, \ldots, M$ measurement taken at points $\mathbf{z}_i^m$. Equation (2.29) now becomes

$$A(\mathbf{z}_1, \mathbf{z}_2) = B(\mathbf{z}_1, \mathbf{z}_2) - \sum_{i,j} B(\mathbf{z}_1, \mathbf{z}_i^m) \Psi^{-1}(\mathbf{z}_i^m, \mathbf{z}_j^m) B(\mathbf{z}_j^m, \mathbf{z}_2). \tag{2.30}$$

Equation (2.30) provides an efficient method to compute $A(\mathbf{z}, \mathbf{z})$ which is already an improvement in terms of computational time over the classical OA method described in Section 2.1. However, given a specific form of the covariance function $B(\mathbf{z}, \mathbf{z}')$, it is possible to do even better by finding an analytical solution to the integral in Eq. (2.19).

We consider the case

$$B(\mathbf{z}, \mathbf{z}') = e^{-\frac{(\mathbf{x}-\mathbf{x}')^2}{\sigma^2} - \frac{(\mathbf{y}-\mathbf{y}')^2}{\sigma^2} - \frac{(\mathbf{t}-\mathbf{t}')^2}{\tau^2}}.$$

σ and τ here refer to the spatial and temporal scales associated with the ocean, but from the numerical point of view they do not have to have any physical significance. By choosing such form of covariance function, Equation (2.30)

gives

$$A(\mathbf{z},\mathbf{z}) = 1 - \sum_{ij} \Psi^{-1}(\mathbf{z}_i^m, \mathbf{z}_j^m) e^{-\frac{(x-x_i^m)^2}{\sigma^2} - \frac{(y-y_i^m)^2}{\sigma^2} - \frac{(t-t_i^m)^2}{\tau^2} - \frac{(x-x_j^m)^2}{\sigma^2} - \frac{(y-y_j^m)^2}{\sigma^2} - \frac{(t-t_j^m)^2}{\tau^2}}. \tag{2.31}$$

Performing some algebraic manipulations we see that

$$\begin{aligned} \frac{(x-x_i^m)^2}{\sigma^2} + \frac{(x-x_j^m)^2}{\sigma^2} &= \frac{2}{\sigma^2}\left[x^2 - 2x\frac{x_i^m + x_j^m}{2} + \left[\frac{x_i^m + x_j^m}{2}\right]^2 + \left[\frac{x_i^m - x_j^m}{2}\right]^2\right] \\ &= \frac{2}{\sigma^2}\left[x - \frac{x_i^m + x_j^m}{2}\right]^2 + \frac{1}{2\sigma^2}(x_i^m - x_j^m)^2 \end{aligned} \tag{2.32}$$

Therefore, Eq. (2.31) is equivalent to

$$\begin{aligned} \|A\| &= \sum_{ij} \Psi^{-1}(\mathbf{z}_i^m, \mathbf{z}_j^m) e^{-\frac{(x_i^m - x_j^m)^2}{2\sigma^2} - \frac{(y_i^m - y_j^m)^2}{2\sigma^2} - \frac{(t_i^m - t_j^m)^2}{2\tau^2}} \\ &\quad \times \int d\mathbf{z}\; e^{-\frac{\left(x - \frac{x_i^m + x_j^m}{2}\right)^2}{(\sigma/\sqrt{2})^2}} e^{-\frac{\left(y - \frac{y_i^m + y_j^m}{2}\right)^2}{(\sigma/\sqrt{2})^2}} e^{-\frac{\left(t - \frac{t_i^m + t_j^m}{2}\right)^2}{(\tau/\sqrt{2})^2}}. \end{aligned} \tag{2.33}$$

The only task that is left to do at this point is to solve the integrals. In Chapter 3 we are using the quantity in Eq. (2.33) as a metric to evaluate the performance of the sampling trajectories. Although the integral in Eq. (2.33) could be a challenge to solve on complicated domains, in this work we only apply it to square domains: $(x, y, t) \in [-D_x, D_x] \times [-D_y, D_y] \times [-D_t, D_t]$. Under those

simple domains the value of the OA metric can be computed as

$$\begin{aligned}
\|A\| &= \sum_{ij} \Psi^{-1}(\mathbf{z}_i^m, \mathbf{z}_j^m)\; e^{-\frac{(x_i^m - x_j^m)^2}{2\sigma^2} - \frac{(y_i^m - y_j^m)^2}{2\sigma^2} - \frac{(t_i^m - t_j^m)^2}{2\tau^2}} \\
&\quad \times \int_{-D_x}^{D_x} dx\; e^{-\frac{\left(x - \frac{x_i^m + x_j^m}{2}\right)^2}{(\sigma/\sqrt{2})^2}} \int_{-D_y}^{D_y} dy\; e^{-\frac{\left(y - \frac{y_i^m + y_j^m}{2}\right)^2}{(\sigma/\sqrt{2})^2}} \int_{-D_t}^{D_t} dt\; e^{-\frac{\left(t - \frac{t_i^m + t_j^m}{2}\right)^2}{(\tau/\sqrt{2})^2}} \qquad (2.34) \\
&= \frac{\sigma^2\tau}{64}(2\pi)^{\frac{3}{2}} \sum_{ij} \Psi^{-1}(\mathbf{z}_i^m, \mathbf{z}_j^m)\; e^{-\frac{(x_i^m - x_j^m)^2}{2\sigma^2} - \frac{(y_i^m - y_j^m)^2}{2\sigma^2} - \frac{(t_i^m - t_j^m)^2}{2\tau^2}} \\
&\quad \times \left[\operatorname{erf}\left(\frac{\sqrt{2}}{\sigma} \left(D_x - \frac{x_i^m + x_j^m}{2} \right) \right) + \operatorname{erf}\left(\frac{\sqrt{2}}{\sigma} \left(D_x + \frac{x_i^m + x_j^m}{2} \right) \right) \right] \\
&\quad \times \left[\operatorname{erf}\left(\frac{\sqrt{2}}{\sigma} \left(D_y - \frac{y_i^m + y_j^m}{2} \right) \right) + \operatorname{erf}\left(\frac{\sqrt{2}}{\sigma} \left(D_y + \frac{y_i^m + y_j^m}{2} \right) \right) \right] \\
&\quad \times \left[\operatorname{erf}\left(\frac{\sqrt{2}}{\tau} \left(D_t - \frac{t_i^m + t_j^m}{2} \right) \right) + \operatorname{erf}\left(\frac{\sqrt{2}}{\tau} \left(D_t + \frac{t_i^m + t_j^m}{2} \right) \right) \right] \qquad (2.35)
\end{aligned}$$

where the error function

$$\operatorname{erf}(s) = \frac{2}{\sqrt{\pi}} \int_0^s d\xi\; e^{-\xi^2}$$

is tabulated.

Qualitatively, we have to balance two forces to minimize the metric in Eq. (2.35). On one hand, we need to space the measurements as far as possible (to minimizes the terms $e^{-(\mathbf{z}_i^m - \mathbf{z}_j^m)^2}$) and, at the same time, try to keep the measurements as close to the center of the domain as possible to minimize the terms $\operatorname{erf}(\cdot)$. Equation (2.35) evaluates the metric but does not require the computation of the error map $\mathbf{A}$ at any grid point. A typical sample size necessary to evaluate candidate patterns is $M \sim 300$ measurements. In this case, we need to invert a 300×300 matrix to find Ψ^{-1}. Once this is done, the metric is obtained by a double sum ($M \times M$) where each element only requires the numerical computation of three error functions. The major advantage is the

complete disappearance of N, the number of grid points which is, in extended phase space (i.e. space-time), much larger than M. This lets us compute the metric for one set of trajectories in less than a second. For a $250 \times 250 \times 250$ grid, this new method reduces the computation time needed by the classical OA algorithm by a factor 250^3.

Chapter 3

Optimal Patterns

The goal of this chapter is to define the optimization problem, explain the approach to identify the best sampling patterns for a given region, and to present the results for a class of experiments on simple domains. Objective Analysis (OA) as described in Chapter 2 sets the stage for optimization by giving us a quantitative measure to compare candidate patterns. We characterize the region by spatial and temporal scales used in oceanography as well as dimensionless parameters representing the shape and size of the domain. We then use the OA metric in conjunction with a modified steepest ascent algorithm to identify sampling patterns that perform best for an experiment involving four gliders on a simple domain.

3.1 Structured Sampling Patterns

The underlying question that we seek to answer is: *what is the best way to use multiple sensors to collect data?* In the context of underwater gliders and oceanographic exploration as described in Chapter 1, we need to devise a way to direct gliders so that they collect the richest possible data set for a given

length of experiment. In light of Chapter 2 we know qualitatively that we need to keep the gliders from bunching up and collecting redundant data and, at the same time, prevent them from spreading the measurements too far apart in space and time in order to have greater certainty in interpolating the data. Note that this work is specialized to the plane, so the patterns discussed below should be interpreted as 2D.

Using the OA metric as a quantitative measure of richness of the data set, it is conceivable to devise control laws that would take into account the distances between measurements in space and time, and would drive the gliders away from each other when they are clustered and pull them back if they get far apart. This would produce irregular paths, resembling a bowl of noodles. Although the performance of such control methods might be comparable to the Structured Sampling Patterns that we propose here, such an approach has a number of disadvantages which we briefly mention below to motivate the work in this thesis. *Structured* Sampling Patterns are pre-determined closed tracks that would be traversed by gliders. Here the control effort is directed to keep the gliders moving along the tracks, and it is decoupled from the performance optimization. We contrast this idea with *gradient type* algorithms where control decisions for each glider are made upon evaluation of current distribution of other gliders and a low-level performance optimization is performed 'on the fly'. Examples of a gradient type approach using the ideas of computational geometry and Voronoi partitions can be found in [8] and [9], and yet another take on the coverage problems that can be viewed as an alternative to what is presented here is described in [26].

A structured approach allows us to simplify the coverage problem and make it more suitable for systematic study. Instead of being faced with a decision how to proceed further for optimal sampling performance every time a glider

surfaces, we decouple the problem into two parts: (1) design of the tracks and (2) control of the gliders to the tracks during the experiment. By dealing with optimization of patterns separately, not only do we take away the computational burden from routine operations during observation, but we also allow analytical solution through introduction of parameters and a more systematic analysis of performance using repeatable paths.

Another important issue is the effectiveness and reliability of the method. OA metric evaluation is inherently a computationally costly procedure, and it becomes even slower and more cumbersome as the number of sensors in the network and sampling time increases. If such analysis is necessary every time a glider surfaces and needs new waypoints, such control system will quickly become impractical as the gliders would waste a lot of time waiting for instructions. In the case of structured patterns, such analysis involving OA metric evaluation is done only once, when the shape of the patterns is determined via optimization for a given set of oceanographic parameters. During the course of an experiment, a much more quickly computed set of control laws, designed to keep the gliders on tracks, provides them with new waypoints without the need for evaluation of the OA metric.

In the context of oceanographic exploration, data collected on repeated tracks are more meaningful than that from random places in the domain. Some of the tools for analyzing fluxes and large scale currents were developed for sensor platforms with limited mobility such as instruments dragged behind ships (see for example [14] and [2]). In those experiments data was collected on straight lines or 'lawn mower patterns' (see Section 3.3 for details about such patterns). As a consequence, the current generation of experts in the field is accustomed to working with this kind of data.

3.1.1 Problem Definition

Although we are strongly motivated by the application of this work to underwater gliders, we want to keep our assumptions as general as possible to allow application of this work to other coverage problems. Keeping the assumptions as close to reality as possible, we introduce a certain degree of abstraction and simplification to make the problem tractable. For the purposes of this study, we impose the following constraints:

1. In light of the discussion in Section 3.1, we must have *Structured patterns*, meaning that they will be determined for the entire length of experiment and expressed using parameters. In addition, in order to derive some predictable and repeatable results, we require that the patterns are *periodic*. In other words, the spatial distribution of the gliders at some time t_1 in the domain must repeat itself at some later time $t_2 = t_1 + T$, for fixed $T > 0$.

2. We have *four gliders* moving at *equal and uniform speed*. The absolute speed itself is of little importance, but rather its relation to the ratio of spatial and temporal scales of the sampled field. The assumptions that (1) all gliders are moving at the same speed and (2) their speed does not change throughout their trajectory are important. The first is consistent with the underwater gliders used in the Monterey Bay experiments (see Chapter 1). The second, on the other hand, is a simplification of the current study and in fact it is one of the shortfalls of this work. One can imagine that in the presence of currents and other disturbances in the real ocean, a glider's effective speed would not be uniform throughout its trajectory, even if the 'still water' speed remains constant. The number of the gliders is chosen as a compromise between a generality of the results

and computational complexity. Four gliders is not as much of a special case for the coverage problem as it might seem. In Appendix A we present results for two- and three-glider formations from which we see that the results for fewer gliders are similar to those for four, with obvious limitations. Small domains with more than four gliders become crowded and the advantages of using smart coverage methods diminish: with overwhelming number of sensors any coverage method will give acceptable results. For large domains on the other hand, using very long tracks that span the entire domain becomes impractical, so the large domains cold be split up into smaller subdomains covered by four or fewer gliders.

The requirement that the patterns must be periodic implies that the paths must be some sort of a closed shape. The approach that we take in this thesis is to use elliptical tracks parameterized by the location of the center (C_x, C_y) and size of semimajor and semiminor axes denoted by a and b respectively. Paley et. al in papers such as [31] describes control laws to an even more general shape called the superellipse, a rounded rectangle formed by using exponent $p > 2$ in Eq. (3.1).

$$\left|\frac{x}{a}\right|^p + \left|\frac{y}{b}\right|^p = 1. \tag{3.1}$$

$p = 2$ gives the formula for a regular ellipse that we use in this study. With $a = b$ it becomes a circle and with $a \gg b$ or $a \ll b$ we can approximate a linear path.

3.1.2 Parameters

Suppose we have gliders and want to design elliptical tracks that they will follow. The parameters that we will optimize over include the following:

1. The relative phases of the gliders θ_{jk}.

2. Center of each elliptical track $C_k = (x_k, y_k)$. Note that in general each glider will follow its own track, but if the tracks are the same, several gliders may effectively follow the same track.

3. Shape parameters a_k and b_k corresponding to the semimajor and semiminor axes of ellipses.

All together we have 4 shape parameters per glider plus 3 relative phases, which for four gliders makes it 19 parameters to optimize over. Even with the fast OA metric evaluation derived in Chapter 2, this is a lot. By running a crude-resolution optimization (see Section 3.2) and observing preliminary results, we were able to extract certain characteristics of those results and reduce the parameter set.

First of all, we note that in order to have periodic patterns, the perimeters of all tracks must either be equal (we refer to such patterns as *single-beat patterns* because the period of each glider is the same), or one should be a rational multiple of the other, such as $\frac{1}{2}$ or $\frac{2}{3}$, which we later define as 1-2 and 2-3 *resonance patterns* respectively. We distinguish the single-beat versus the resonance cases and study them separately. For each of those cases, once the parameters a and b are picked for one track, the perimeter of the ellipses is set for all the rest. In this case we only vary a for other tracks while b is determined by the choice of a to ensure the proper perimeter.

We also noticed that because of the symmetry of the domain, under certain combinations of spatial and temporal scales, the optimization algorithm would align the centers of the tracks along the line of symmetry of the domain. We study those cases as a subclass by locking the x_k component of the centers, while varying y_k.

For some combination of the scales we noticed that the optimal pattern would be such that the centers of the tracks aligned symmetrically with respect to the center of the domain as in Figure 3.1. This gave rise to another reduced-parameter case where we fixed the centers of the tracks on the vertices of the square inscribed in the domain such that its center coincides with the center of the domain. We varied the length of the edge l of the inscribed square, which determined C_k for all tracks.

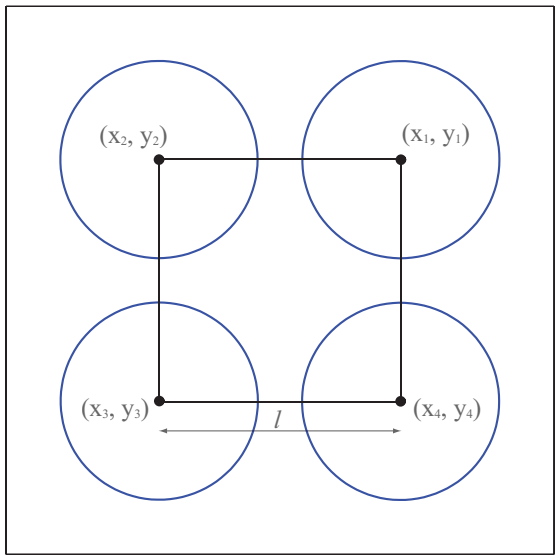

Figure 3.1: Sampling trajectory with centers of the four tracks symmetrically distributed with respect to the center of domain.

Lastly, during the preliminary optimizations, we saw some patterns when two or more gliders would occupy the same track, always $\frac{2\pi}{M}$ out of phase where M is the number of gliders on the combined track. Trying out several combinations of multiple gliders coupled to one track and comparing the resulting metrics, we came to conclusion that 'two and two' configuration for single beat patterns (two tracks with two gliders on each) was the only pattern that has advantage over all other patterns for certain parameter values. We then studied this subclass in more detail by pairing the gliders and optimizing over only two

sets of shape and center parameters and three relative phases. The resulting classes of patterns are summarized in Figure 3.2.

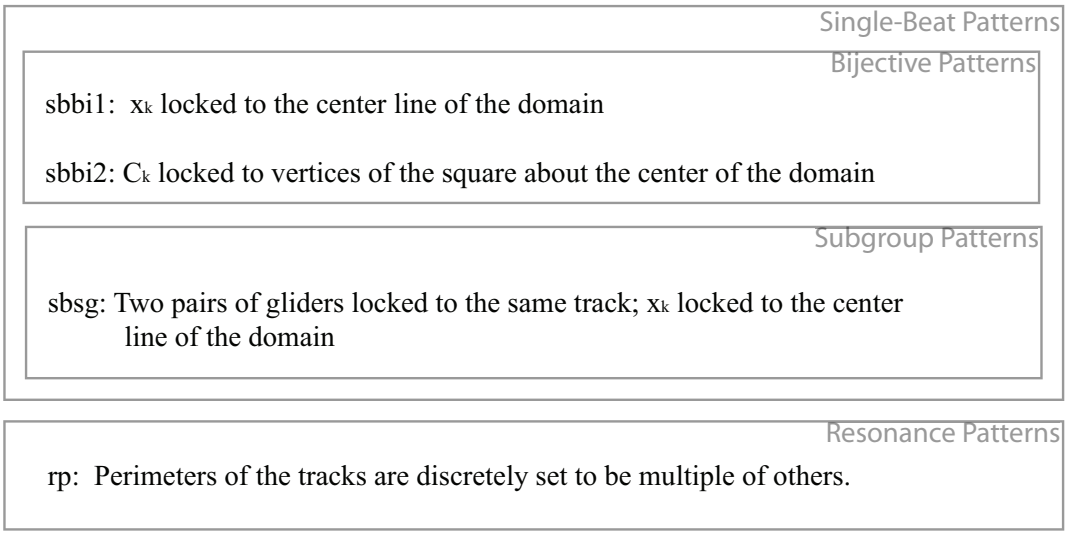

Figure 3.2: Optimization of parameter sets and resulting classes of Structured Sampling patterns.

3.1.3 Decorrelation scales

When studying various oceanographic phenomena, one has to look at how the variability in collected data is significant between different measurement sites as well as between measurements at the same site, but taken at different times. In other words, one has to have an estimate of the typical size and 'life time' of coherent features such temperature fronts and eddies. Such statistical measure in oceanography is often referred to as the *decorrelation scales*, which indicate the distance and time over which variations in data become decorrelated.

The Gaussian form of correlation function assumed in the development of the Objective Analysis method (Chapter 2) gives rise to the e-folding decorrelation scales, meaning that the distance and time at which the correlation reaches $1/e \approx 37\%$ is set to be σ and τ respectively. For instance, during the AOSN

experiment in Monterey Bay the scales were computed to be $\sigma = 25$ km and $\tau = 2.5$ days [23] using the data collected by the underwater gliders during the experiment decribed in [35]. An intuitive view of the decorrelation scales is *how useful is a new data point.* Suppose we make a new measurement that is removed a distance d from other measurements. If d is much larger than σ, it is not too useful in the sense of richness of the data set since the size of the features under investigation is small and we cannot resolve it with measurements spread so far apart. Similarly, if the measurement is taken time t after the previous one at this location, and $t \gg \tau$ the last measurement is too old and we can no longer resolve what happened during time t. The scales are computed empirically and, in general, would be different for different regions of the ocean and different features studied in the experiment (see for example [35] and [11]). Note that in a semi-enclosed body of water such as the Monterey Bay, decorrelation scales are somewhat different from what one would expect in the open ocean. Notably, [40] presents an analysis of temporal decorrelation scales in the open ocean and comes up with somewhat longer decorrelation scales ($\sigma = 50$ km and $\tau = 6$ days). Poulain and Niiler in [33] consider Lagrangian drifter trajectories offshore of Coastal California and get a spatial scale of $40 - 50$ km and a temporal scale of $7 - 10$ days.

Although much of the work in this thesis is motivated by the AOSN and ASAP experiments in Monterey Bay for which the scales have been computed and can be used as parameters for optimization of sampling trajectories, we extend the work done previously by studying the optimal patterns *as a function of decorrelation scales.* The purpose of the further development, application of OA methods and optimization is *to provide insight into which patterns would perform best to collect data in various environments.* This is an important piece of information if one is considering applying the techniques of ocean exploration

using a network of mobile sensors to other fields. Decorrelation scales in the atmosphere for example are very different from those in the ocean [4], and the sampling paths producing the richest data sets would be different. In this sense, the work presented in this thesis facilitates cross-discipline transition of sampling techniques developed for underwater gliders.

Performing optimization over a range of decorrelation scales and parameters described in Section 3.1.2 allowed us to identify patterns that perform best on subsets of scale domain. Figure 3.3 shows a plot of OA metric values of several patterns and how they compare for different values of σ and τ. It is clear that performance of one pattern relative to others varies depending on what scales apply. Careful study of patterns and subsets of parameter space allow us solve the inverse problem where we will be able to tell which pattern is the best for a given set of oceanographic parameters.

It turns out that the use of σ and τ is slightly limiting in terms of applicability of results, because in such a representation, results depend on specific parameters of the experiment such as size and shape of the domain and duration of the experiment. In order to represent results independent of those variables, we consider dimensionless parameters as developed in [23]. Defining $\mathcal{B}_a$ and $\mathcal{B}_b$ as width and height of the domain, and $\mathcal{T}$ as the duration of the experiment, let the dimensionless parameters be

- $S\mathfrak{z} = \sqrt{\mathcal{B}_a \mathcal{B}_b}/\sigma$ to represent the size of the domain,
- $S\mathfrak{t} = \mathcal{T}/\tau$ for sampling time interval
- $S\mathfrak{h} = \mathcal{B}_b/\mathcal{B}_a$ for shape of the domain, and
- $S\mathfrak{p} = v\tau/\sigma$ for normalized speed of the vehicle.

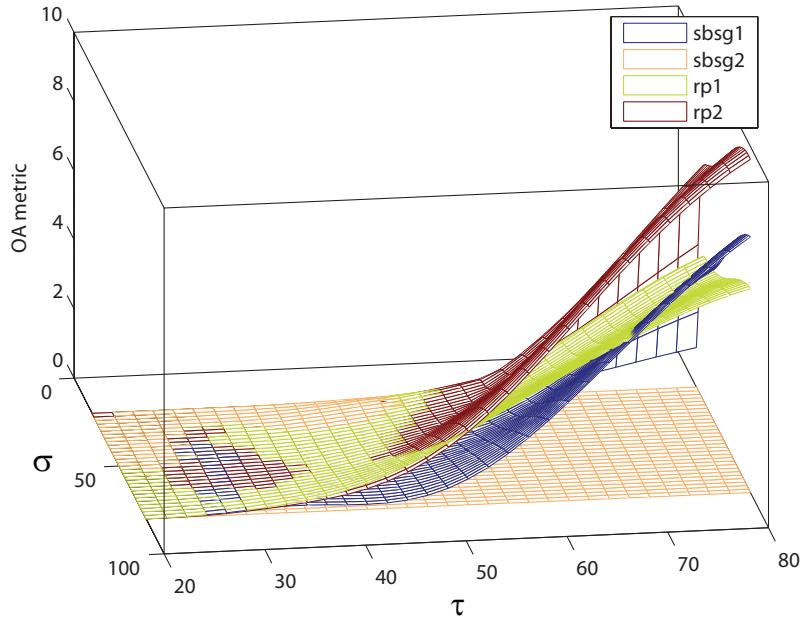

Figure 3.3: OA metric surfaces representing performance of various patterns over (σ, τ) grid for $100\mathsf{d} \times 100\mathsf{d}$ square domain and $v = 1\ \mathsf{d/t}$, $\mathcal{T} = 1000\mathsf{t}$. Substituting d = km and t = hours provides a reasonable representation for typical gliders.

3.2 Optimization Routine

The OA metric as described in Chapter 2 gives a measure of richness of information collected given a list of positions and times of measurements sites. It does not matter what quantity we are measuring or what the values are, just the fact that a measurement has been acquired at certain points. When we propose a candidate pattern, we specify the parameters of the tracks (C_k, a_k, b_k) as well as the relative phases for each pair of gliders θ_{jk}. We then simulate their motion and record the measurement sites along their respective tracks, assuming that the gliders follow their tracks exactly. This information gets passed to the OA metric evaluation routine which outputs a scalar telling us the level of certainty that the recreated field is correct. Equivalently one can compute the level of uncertainty (estimation error), but in this work recording certainty seemed more

intuitive. If this certainty value is better than the previous one, we update our notion of best pattern and make the next optimization step.

Let d be an arbitrary unit of distance and t be an arbitrary unit of time. For various experiments d, for example, can be assigned the units of meters, km, miles, etc. In the actual optimization we used a $100\mathsf{d} \times 100\mathsf{d}$ square domain so $S\mathfrak{h} = 1$ was held constant. The parameter $S\mathfrak{p}$ was not fixed. Instead the speed of the vehicles was set to be 1 d/t, while the duration of the experiments was set to be $\mathcal{T} = 1000\mathsf{t}$. The frequency of sampling along the track was chosen to be 1 measurement per t, and the range of decorrelation scales was set [1 - 100] for both σ and τ in units of d and t, respectively. The idea here is that the values of σ and τ for a real experiment would fall somewhere between the spacing between individual measurements and the size of the domain being sampled. A choice of d = km and t = hours makes for a reasonable evaluation of typical underwater gliders.

To find the pattern that produces the richest data set, we have implemented a modified version of the steepest ascent algorithm. For each parameter, we make a small perturbation and note the direction in which the value of the metric increases. Then we propose a new path configuration that incorporates all the incremental improvements for each parameter, recompute the metric, and compare it with the previous value.

Although it is impossible to visualize the parameter space due to its high dimensionality, we know from experiments that it is a pretty 'jagged' space with lots of local extrema. See for example Figure 3.4 where we fixed all parameters except the relative phase of two gliders and plotted the OA metric as a function of the relative phase angle.

As a consequence, simply using the steepest ascent algorithm, it would be very easy to get 'stuck' on one of the local maxima. To combat this situation,

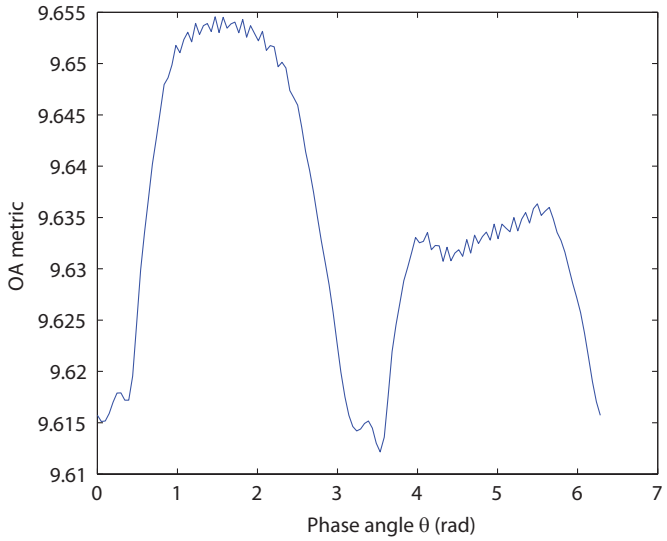

Figure 3.4: OA metric as a function of the relative phase of two gliders.

we created a new mode of the optimization routine where we first make smaller steps in the direction we were headed before, and then, if this fails to find a new peak, we explore the vicinity of the peak with random jumps.

We extensively tested this approach against the 'visualizable' parameter spaces with three or fewer free parameters displaying the optimization results and the calculated matric values on a 3D plot. Although there is no guarantee that this algorithm was able to find the global maximum in all cases, it performed flawlessly in those that we could check.

To generalize the performance of the patterns for different scales, sampling times and speeds, we ran the optimization on a fine grid of parameters $S\mathfrak{z}$ and $S\mathfrak{t}$ and identified in Section 3.1.3 the specific patterns with subsets of parameter space where they perform best.

3.3 Lawn Mower Patterns

To make useful assessment of performance of Structured Sampling Patterns and specifically the elliptical, closed loop approach that we take in this thesis, we compare those to a generalization of the traditional 'lawn mower' approach to coverage problems. With one survey vehicle it has been customary to collect data on the domain via repeating back-and-forth sweeps as those made by a lawn mower (see for example Figure 3.5) [2]. The same patterns are sometimes called 'radiator patterns' in the literature because the shape is reminiscent of radiators [14]. Although it is not obvious how to extend this approach to the situation when we have more than one mobile sensor, we postulate a solution for two-vehicle network and compare its performance to the a two-vehicle symmetric pattern solution developed in this chapter. See Appendix A for two-glider formation optimized patterns.

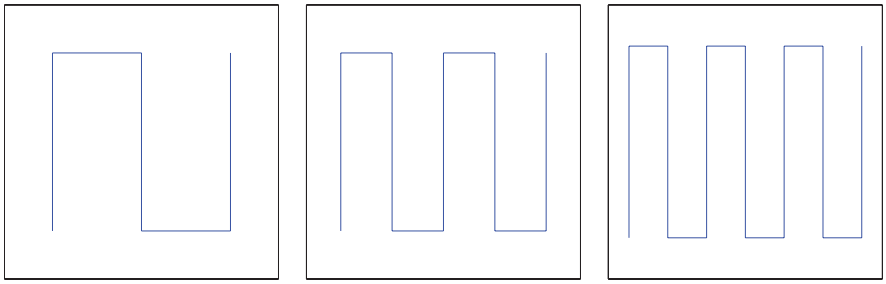

Figure 3.5: Sample Lawn Mower Patterns on square domains. Three passes (n=3) left, five passes (n=5) center, seven passes (n=7) right.

3.3.1 Parameters of the Lawn Mower Pattern

With just one sensor, we can follow a lawn mover track such as in Figure 3.5 to sample the area. There is a number of ways two gliders can utilize the same pattern to collect data on the domain. For example, they can simply follow one another, directly on the track with some defined lag between them.

Alternatively, they can start from the opposite ends of the pattern, meet in the middle and again go off to opposite ends. Another option is to keep them some distance apart, but following the same 'virtual leader' which follows the Lawn Mower Pattern. How they follow the virtual leader is a separate problem and can involve artificial potentials as described by E. Fiorelli and others in [22] and references therein. The solution that we have tried in this thesis is a much simpler one with a static 'rod' of length d pivoted at the center and rotated by the angle θ from the horizontal, so that the center point follows the Lawn Mower pattern (see Figure 3.6 for illustration). We have seen from metric evaluation that even such a simple solution (with d and θ chosen within certain range) performs better than the 'lag' or the 'opposite ends' ways of following the pattern. Since our purpose in considering the Lawn Mower patterns in this thesis is merely to roughly compare its performance to that of symmetric patterns, we use this simple approach here and leave the more sophisticated pattern following schemes for future work.

For simple domains, a Lawn Mower pattern such as in Figure 3.6 can be characterized using the following parameters:

- X width of the pattern
- Y height of the pattern
- n frequency of the passes
- d separation between the sensors (for two-sensor array)
- θ shift angle of the sensors

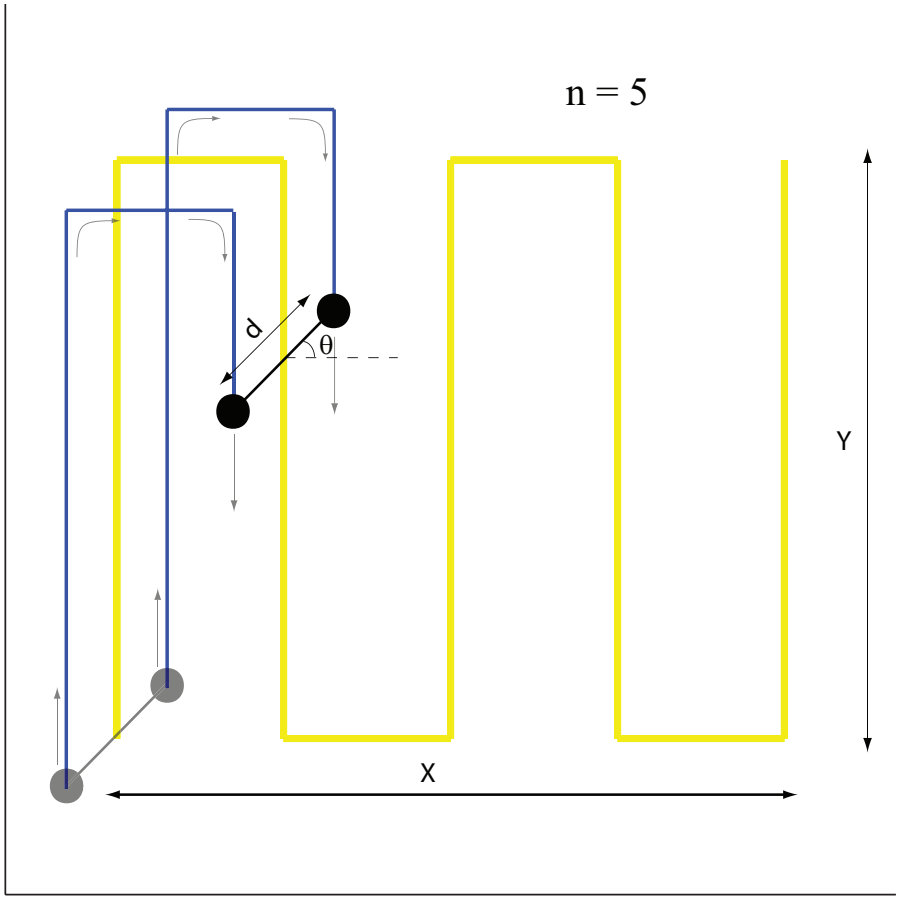

Figure 3.6: Parameters of Lawn Mower Patterns.

3.3.2 Optimization for Lawn Mower Pattern

Essentially we used the same optimization scheme here as we used for symmetric patterns, which facilitates a more direct comparison between the two classes of patterns. Again, we ran the optimization on the grid of parameters $S\mathfrak{z}$ and $S\mathfrak{t}$ and compiled the 'best option for this set of parameters' surface that we show in Figure 3.7. Similar to the case with symmetric patterns where we find that different types of patterns are more suitable for different scales, Lawn Mower patterns with different frequency of passes n were shown to be more appropriate than others for a given range of scales. Since Lawn Mower patterns are not the focus of this thesis and are presented here to benchmark the performance of

the Symmetric patterns, we extend the notion of 'best option for this set of parameters' to include variations in n. In practice this meant that we 'patched together' the surface in (σ, τ) space with segments of maximum metric values across all n. As seen in Figure 3.7 even such 'best option' surface is inferior in performance to a typical symmetric pattern that is optimal on a subset of parameter space. If we were to patch up a similar 'best option surface' for symmetric patterns, the difference would be even more stark. Note that the difference in performance grows with σ and τ. This is due to the fact that the two vehicles in lawn mower pattern are close together while in **sbbi1s** symmetric pattern they are more uniformly spread in the sampled domain. For large σ and τ the ability of symmetric pattern to sample the field at locations that are far apart plays increasingly important role.

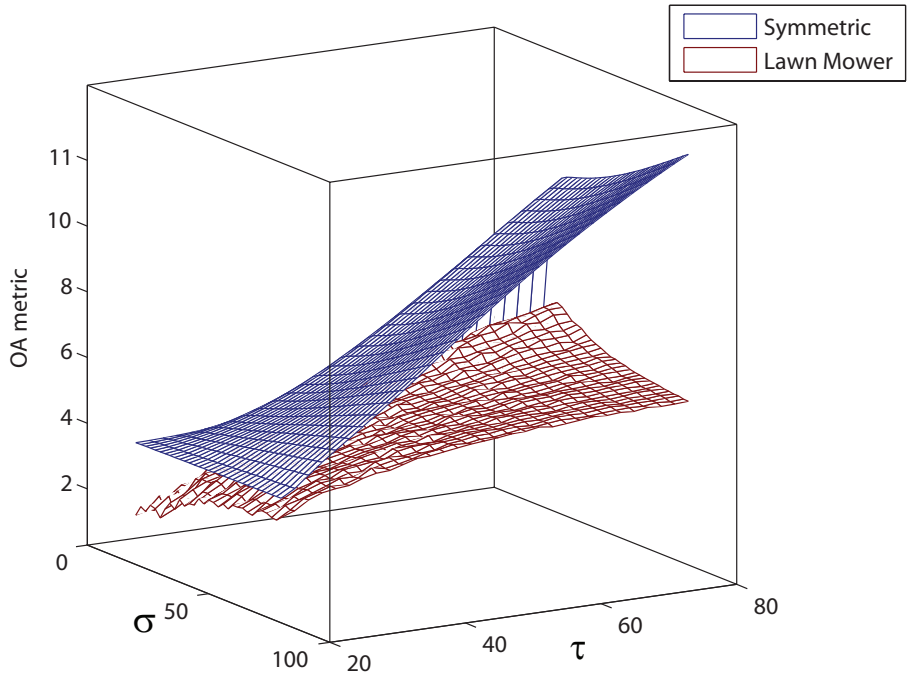

Figure 3.7: Comparison of OA metrics for patched 'best option for this set of parameters' Lawn Mower patterns with two vehicles and comparable **sbbi1s** symmetric pattern for two vehicles (see Appendix A for the shape of the pattern). For this plot we used for $100\mathsf{d} \times 100\mathsf{d}$ square domain and $v = 1\ \mathsf{d/t}$, $\mathcal{T} = 1000\mathsf{t}$.

3.4 Single-Beat and Resonance Patterns

To achieve optimal sampling using Structured Symmetric Sampling patterns, it is necessary to control the gliders so that they are on their tracks and are correctly distributed relative to one another on the tracks. Relative phase of the gliders around closed curves plays an important role and synchronization or balancing of the phases can only be achieved for certain types of patterns. In papers such as [31] and [23], control of the relative phases is developed for the gliders on tracks with equal perimeter. With equal speed along the tracks, phase synchronization can be stabilized. If the perimeters of the tracks are different, the gliders cannot simultaneously be on tracks and stay in phase.

3.4.1 Design and Application

One of the original contributions presented in this thesis is a treatment of a new type of sampling trajectories where gliders are placed on tracks with different perimeter, yet still able to keep synchrony. This is achieved by allowing the perimeters of tracks to differ by rational factors. Figure 3.8 for example shows tracks such that the perimeter of track **B** is 2/3 of **A**, and the perimeter of **C** is 1/3 of **A**. If we were to use those tracks as a candidate sampling trajectory, we would call the pattern a *3-2-1 resonance,* according to the number of segments necessary to return the gliders to the original configuration.

Optimization of pattern configurations involving resonant modes is tricky. It is inherently a discrete problem in a sense that there is no smooth transition between single-beat configuration (length of all tracks is the same) and any resonant mode such that synchrony is attainable at every intermediate step. Once a single-beat pattern is optimized for a set of parameters, it does not make sense to simply change the length of some tracks and see if it performs

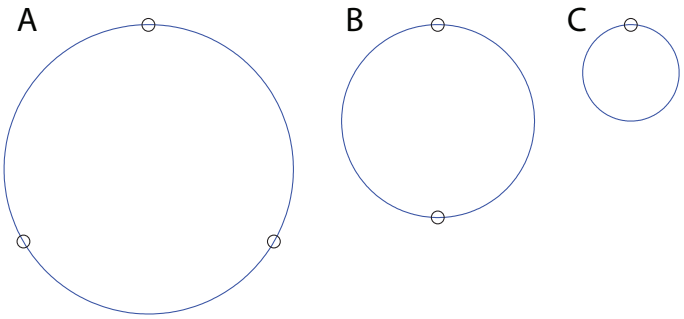

Figure 3.8: Resonance Patterns. Perimeter of **B** is 2/3 of **A**, and perimeter of **C** is 1/3 of **A**. Equal length arcs are marked with small circles.

better. It requires a whole new optimization during which the best shape and location of the tracks is determined. In fact, the author could not come up with anything better than to exhaustively check a number of patterns and compare the resulting performance metric values. A significant improvement to the work presented here would be a more clever way of selecting candidate patterns.

3.4.2 Resonance in the Context of Ocean Sampling

Technically, one can come up with an unlimited number of resonance patterns; perimeters of almost every pair of sampling tracks can be expressed (or approximated) as a fraction of one another making them resonance patterns. We must restrict this in some way so that resonance pattern candidates are meaningful in the context of physical problem. A 31-47 'resonance pattern' for example is not of much use in the real experiment since it would take 31 revolutions of the larger track and 47 revolutions of the smaller track to get in-sync again. The gliders will be effectively unsynchronized and the data collected in such manner will likely be suboptimal. We must set the threshold of what we can call 'synchrony' in the context of the problem. For the optimizations that were done in the current work where each glider goes around its loop 8 to 10 times depending on the length of the path, a reasonable limit would be 4, so that the

original configuration is achieved twice. The resulting combinations 1-4, 1-3, 1-2, 2-3, 3-4 were used as track perimeter restrictions as described in Section 3.1.2.

Note that the resonance pairs 1-2 and 2-4 are the same in the context of the problem. We used this to check the optimization routine since from the point of view of the algorithm, those are different parameters and the location of maxima in OA metric space would be scaled accordingly. As reassurance, optimal track shape parameters and OA metric values for 2-4 resonance were indeed identical to those of 1-2 resonance when appropriately shifted. Similar test was performed for 2-2, 3-3 and 4-4 combinations, which gave results equivalent to single-beat (1-1) patterns.

3.4.3 List of Patterns

In the previous section we made certain assumptions to limit the number of possible resonance patterns. We set the threshold $S = 4$ which effectively limits the time during which we allow the gliders to be out of the desired synchronization. Since the number of possible patterns is equals to how many times the OA optimization will be performed we must assure that this number is minimal. For an N-glider formation with a threshold S, the number of patterns is found by $\left(\binom{S}{N}\right) = \binom{S+N-1}{N}$, where double parentheses denote "S multichoose K", the multiset notation. For four gliders this number is 35, and in the context of the sampling problem can be reduced to 29 by excluding 2-2-2-2, 3-3-3-3, 4-4-4-4 and 2-2-2-4, 2-2-4-4, 2-4-4-4 that are equivalent to 1-1-1-1, 1-1-1-2, 1-1-2-2, 1-2-2-2 respectively. Those can be used to check the optimization algorithm as mentioned in the previous section. The remaining resonance combinations that were used to arrive at results in Section 3.5 are listed in Table 3.1.

1-1-1-2	1-2-2-2	1-3-3-3	2-2-2-3	2-3-3-3	3-3-3-4
1-1-1-3	1-2-2-3	1-3-3-4	2-2-3-3	2-3-3-4	3-3-4-4
1-1-1-4	1-2-2-4	1-3-4-4	2-2-3-4	2-3-4-4	3-4-4-4
1-1-2-2	1-2-3-3	1-4-4-4			
1-1-2-3	1-2-3-4				
1-1-2-4	1-2-4-4				
1-1-3-3					
1-1-3-4					
1-1-4-4					

Table 3.1: Possible resonance patterns for four gliders.

3.5 Results and Implications

Two main results of this thesis are presented in Figures 3.9 and 3.10. Figure 3.9 shows results of the optimization of sampling patterns on the simple domain as described in Section 3.2. The patterns were found to be optimal on a subset of dimensionless parameters $S_{\mathfrak{z}}$ and $S\mathfrak{t}$, and the map identifying each pattern with the subset of parameters is shown in Figure 3.10.

To use this information, one can measure oceanographic quantities such as spatial (σ) and temporal (τ) decorrelation scales in the region of interest via methods such as described in [4] or [11]. Then this information is combined with specific parameters of the experiment, such as size of the domain and length of the experiment to compute the dimensionless quantities $S_{\mathfrak{z}}$ and $S\mathfrak{t}$. Those two values allow to determine the patterns that will work best for this experiment.

Note that the Resonance pattern **rp1** is the best on a relatively large range of parameters compared to other patterns. It is a 1-3-3-3 resonance pattern with phases of the three gliders that share the large loop evenly distributed around the phase space with $\frac{2\pi}{3}$ phase difference. Although not restricted during optimization, the centers of both loops in the optimal solution are collocated at the center of the domain. The other resonance pattern that was found to be optimal on a subset of parameter space, **rp2**, is a 1-1-2-2 resonance where

two gliders on the larger loop are π out of phase. Here again, the optimization process has placed the center of the larger loop on the center of the domain.

Note that the location marked by Δ^1 on Figure 3.10 corresponds to parameter values in the Monterey Bay field experiments with the actual gliders (see Section 1.3.2) where decorrelation scales were estimated to be $\sigma = 25$ km and $\tau = 60$ hours, and glider speeds are approximately 1 km/hr [23]. Location marked by Δ^2 corresponds to a similar domain size experiment in the air with $\sigma = 10$ km and $\tau = 20$ hours [17]. Note that for the 2006 ASAP field experiment in Monterey Bay a pattern most resembling **sbsg1** was used to collect the data. According to our results however, the performance of the array would be better if the gliders would be controlled to **sbbi2b** or **rp1**.

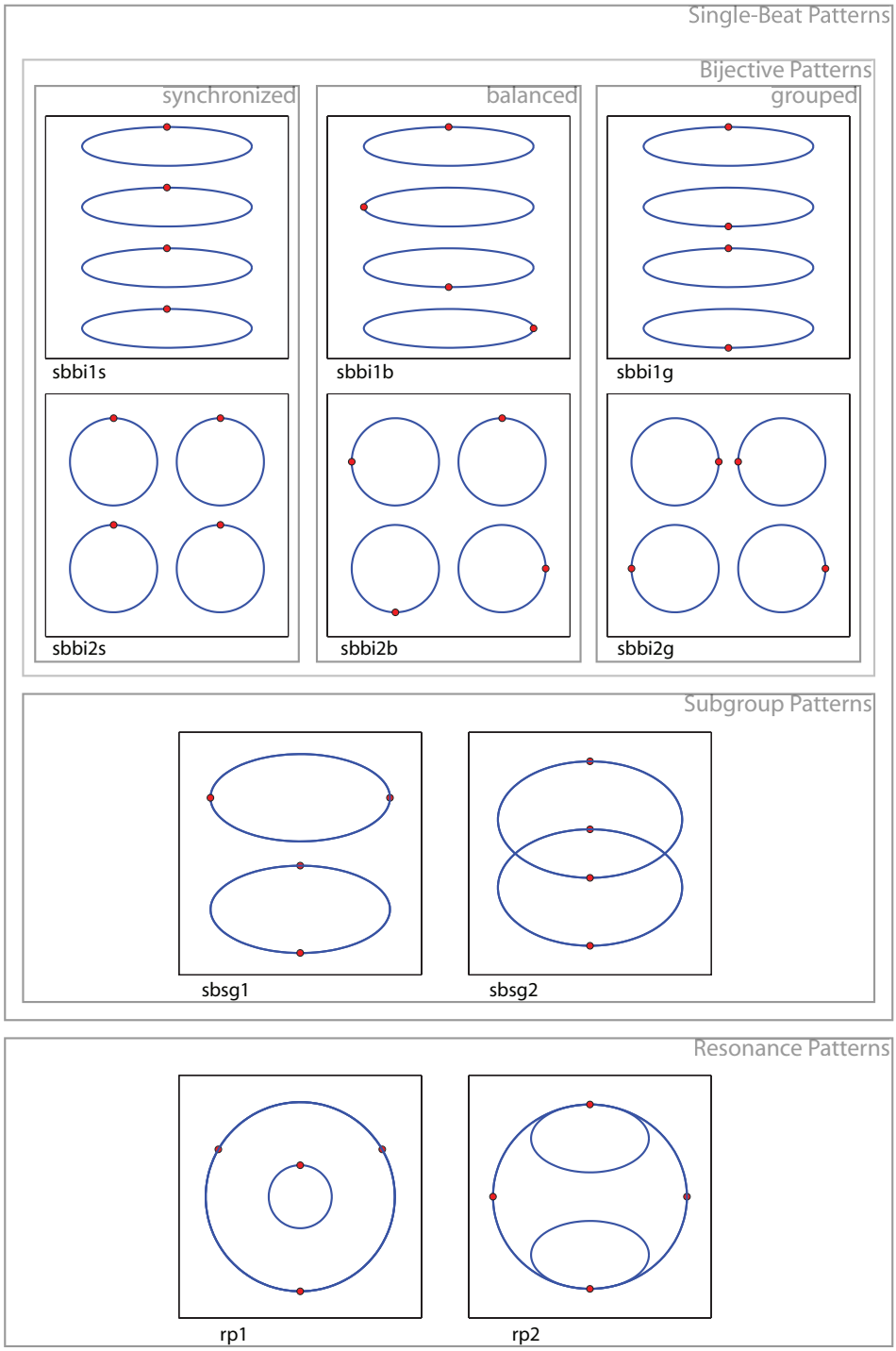

Figure 3.9: Classification of optimized symmetric patterns.

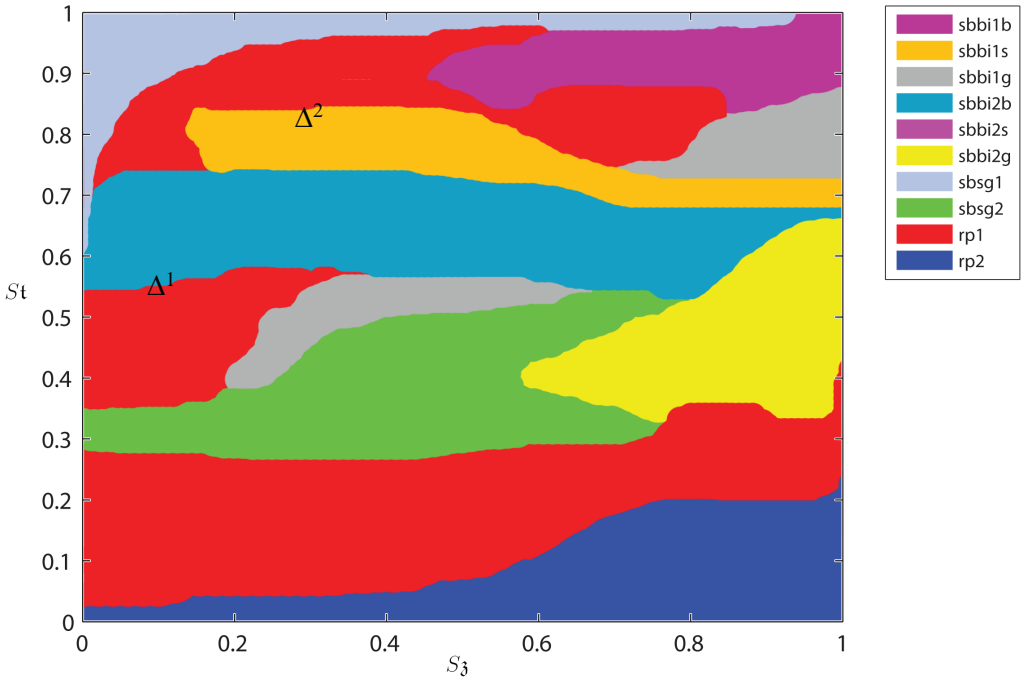

Figure 3.10: Best patterns on the grid of parameters $S\mathfrak{z}$ and $S\mathfrak{t}$ corresponding to the patterns classified in Figure 3.9. Δ^1 corresponds to the AOSN-II experiment in Monterey Bay (see Section 1.3.2) and Δ^2 corresponds to a similar-scale experiment in the air with $\sigma = 10$ km and $\tau = 20$ hours [17]

Chapter 4

Control and Resonance Patterns

In Chapter 3 we suggested the use of structured sampling patterns that allow us to decouple the control problem into two separate parts: design of the tracks and control of the gliders to those tracks. We also performed analysis and arrived at families of patterns most appropriate for specific types of experiments, which satisfies the first part of the control problem. In this chapter we focus on the second part - controls to stabilize the selected patterns. First we review some of the published results on control of the gliders to single-beat patterns (as described in Chapter 3), and provide references for a more in-depth study of the topic. Next, we suggest an extension of that work that deals with control to *resonance* patterns and relate this new approach to existing methods.

4.1 From Oscillator Models to Collective Motion

Following the Kuramoto approach as outlined in Section 1.2.1, we think about the individual gliders as phase oscillators and the collection of gliders as a network of coupled oscillators. The phase here refers simply to the direction in which a particular glider is headed at constant speed. When the oscillators are

in phase, gliders are headed in the same way, hence they are *synchronized*. The other interesting family of equilibrium states occurs when the oscillators are anti-synchronized. In this case, the phases of the oscillators are (in general) randomly distributed around the unit circle so that their centroid is at the origin[1]. It is important to note that in such anti-synchronized state the collective of particles has a fixed center of mass.

One of the core contribution of the work presented in this thesis to sampling technologies using mobile sensor networks is the introduction and analysis of the resonance patterns presented in Chapter 3. In order for those methods to be useful in science, we must provide a method to control the gliders in a way that enables them to follow resonance-type patterns. As we will see shortly, the existing control laws presented in [36], [37] and other papers by Professor Leonard's group have components that are responsible for (1) driving the gliders to a track of specified shape and (2) making sure gliders maintain the prescribed relative phasing around those tracks. Since the *shape* of the resonance patterns presented in this thesis is the same as that used for regular formations, the same shape controls can be used for resonance patterns. The phase control, on the other hand, would have to be different, since in the case of resonance patterns the notions of 'synchronization' and 'balancing' are modified. Therefore, we focus our attention in this chapter on the *phase* component of the control law for resonance patterns. To familiarize the reader with notation and general terminology, we briefly review the *particle model* and phase controls associated with single-beat tracks. We have used elliptical shapes throughout Chapter 3 to derive optimal patterns for sampling, but for readability of this thesis we further

[1]Referring back to Chapter 3 where we present results of the optimization of the sampling patterns we see that among *optimal* patterns we find both synchronized and anti-synchronized configurations. Note also that anti-synchronized patterns are not randomly distributed in phase space, but rather *evenly* distributed (balanced) or congregations of gliders are evenly distributed (grouped). This of course is a subclass of anti-synchronized states.

focus our attention here to *circular patterns.* Our approach to controls is much more intuitively described by considering this special case in the shape space. The extension to ellipses and even to a more general shape, the superellipse, is fairly straight-forward (but messy) and is described in [31] as well as in greater detail D. Paley's PhD thesis [30].

4.2 Single-Beat Patterns

Throughout this chapter we regard the individual gliders as point-mass particles with unit mass. Hence, we sometimes refer to a model that ignores individual glider dynamics as the particle model. Here, we review some of the results that were extensively studied by N. E. Leonard group at Princeton and colleagues (see for example [23], [32], [31], and references therein) as well as elsewhere [18] and [9]. The work in those papers builds on the fundamental discoveries in the field of coupled oscillators by Kuramoto and others in [16] and [20]. See Section 1.2 for a brief treatment of the major developments in this field. The reader is also referred to an article by Steven H. Strogatz [39] that nicely summarizes the results and challenges in the field of coupled oscillators.

4.2.1 Particle Model

Consider N particles of unit mass, characterized by their position and heading and traveling at unit speed. We require that the particles maneuver only by steering and not by speeding up or slowing down. The position of the k^{th} particle is a pair of numbers in the XY plane, which for conciseness we represent in complex notation $r_k = x_k + iy_k$, $r_k \in \mathbb{C} \approx \mathbb{R}^2$. Similarly, we represent the velocity of the k^{th} particle moving at unit speed as $e^{i\theta_k} = \cos\theta_k + i\sin\theta_k$ where $\theta_k \in \mathbb{S}^1$, the unit circle, and $\boldsymbol{\theta} = (\theta_1, \ldots, \theta_N)^T \in \mathbb{T}^N$, the N-torus.

We denote the steering control u_k, which is a feedback control law that is a function of particle position and heading. We use bold to indicate a complex vector such as $\mathbf{r} = (r_1, \ldots, r_N)^\top$ and we denote the Hermitian inner product as $< \mathbf{x}, \mathbf{y} >= \mathrm{Re}\{\mathbf{x}^*\mathbf{y}\}$, where $\mathbf{x}$,$\mathbf{y} \in \mathbb{C}^n$, $n \in \mathbb{N}$, and * is the conjugate transpose. Using this notation, we express the particle model as the following continuous-time system:

$$\begin{aligned} \dot{r}_k &= e^{i\theta_k} \\ \dot{\theta}_k &= u_k, \quad k = 1, \ldots, N. \end{aligned} \tag{4.1}$$

With simple control inputs the behavior of the model is easily visualized. For instance, if the control is constant and zero, that is $u_k = 0$ for all k, then each particle moves in a straight line in the direction it was initially pointing. If the control is constant but not zero, $u_k = \omega_0 \neq 0$, then each particle travels around the circle with radius $|\omega_0|^{-1}$. To allow for more complex behaviors, in the next section we seek to derive u_k with desired properties.

It is useful to independently consider the subsystem of particle headings (phases[2]). Effectively we split the control input u_k into three terms: a constant term ω_0, the spacing control u_k^{spac} and the phase control u_k^{phase}.

$$u_k = \omega_0 + u_k^{spac}(\mathbf{r}, \boldsymbol{\theta}) + u_k^{phase}(\boldsymbol{\theta}), \quad \omega_0 \in \mathbb{R}, \quad k = 1, \ldots, N. \tag{4.2}$$

We further restrict the steering control to be a function only of *relative* positions and headings denoting them $e^{-i\theta_k} r_{kj} = e^{-i\theta_k}(r_k - r_j)$ and $\theta_{kj} = \theta_k - \theta_j$ respectively. Controls of this form preserve the continuous symmetries of Eq. (4.1) that make it invariant to rigid rotation and translation of the particle group [32].

[2]Note that in this context phases represent the headings.

4.2.2 Phase Control for Single Beat Patterns

In this section we focus our attention on studying the *phase model* following [36]:

$$\dot{\theta}_k = u_k = \omega_0 + u_k^{phase}(\boldsymbol{\theta}). \tag{4.3}$$

As in Kuramoto model [20], we introduce the *order parameter*:

$$p\left(\boldsymbol{\theta}\right) = \frac{1}{N}\sum_{k=1}^{N} e^{i\theta_k}. \tag{4.4}$$

We note that controlling the linear momentum of the group in the particle model is equivalent to controlling the coherence of particle phases in the phase model. For that purpose we introduce the following rotationally symmetric phase potential:

$$U_1(\boldsymbol{\theta}) = \frac{N}{2}|p(\boldsymbol{\theta})|^2. \tag{4.5}$$

Being proportional to the square of the order parameter (4.4), the phase potential is maximum for synchronized phase arrangements where $p(\theta) = 1$, and minimum for balanced phase arrangements where $p(\theta) = 0$. The gradient of $U_1(\boldsymbol{\theta})$ is given by

$$\frac{\partial U_1}{\partial \theta_k} =< ie^{i\theta_k}, p(\boldsymbol{\theta}) >, \quad k = 1, \ldots, N. \tag{4.6}$$

Since $U_1(\boldsymbol{\theta})$ is rotationally symmetric, it is invariant to rigid rotations of particle phases, so its gradient is orthogonal to $\mathbf{1} = (1, 1, \ldots)^\top$:

$$\frac{\partial U_1}{\partial \boldsymbol{\theta}}^\top \mathbf{1} = \sum_{k=1}^{N} < ie^{i\theta_k}, p(\boldsymbol{\theta}) >= N < ip(\boldsymbol{\theta}), p(\boldsymbol{\theta}) >= 0. \tag{4.7}$$

We choose the heading control in the phase model (4.3) to be the signed gradient of $U_1(\boldsymbol{\theta})$,

$$u_k^{phase} = -K_1 < ie^{i\theta_k}, p(\boldsymbol{\theta}) >, \quad K_1 \neq 0, \quad k = 1, \ldots, N. \tag{4.8}$$

Putting pieces together we obtain

$$\dot{U}_1(\boldsymbol{\theta}) = \frac{\partial U_1}{\partial \boldsymbol{\theta}}^T \dot{\boldsymbol{\theta}} = -K_1 \sum_{k=1}^{N} < ie^{i\theta_k}, p(\boldsymbol{\theta}) >^2,$$

which is needed to prove the Lyapunov stability of the model. And finally, using the definition of $p(\boldsymbol{\theta})$ in (4.4) we note that the gradient control (4.8) is equivalent to

$$\dot{\theta}_k = \omega_0 + \frac{K_1}{N} \sum_{j=1}^{N} \sin \theta_{kj}. \tag{4.9}$$

which is a simplified version of Kuramoto model [20] for $K_1 < 0$, which stabilizes synchronized phase arrangements.

Implicit in control (4.8) is the assumption that each particle has access to the relative heading of every other particle in computing its own heading, which is often referred to as 'all-to-all communication' in literature [36]. Clearly this would not be true at all times during a real experiment where gliders establish communication only when they surface. This issue is solved using *interconnection graphs* that describe which relative headings and positions are available to each particle for feedback. Such models are often referred to as 'particle models with limited communications' and described in detail in papers such as [32] and [37].

4.2.3 Spacing Control for Single-Beat Patterns

In contrast to the *phase* control presented in the previous section, we now review a *spacing* control that achieves convergence of the particles to a circular track following [36]. We start our analysis with the observation that under the constant control $u_k = \omega_0 \neq 0$, each particle travels at constant, unit speed on a circle of radius $\rho_0 = |\omega_0|^{-1}$. The center of the circle traversed by particle k is $c_k = r_k + i\omega_0^{-1} e^{i\theta_k}$. Multiplied by the constant factor $-i\omega_0$, c_k becomes

$$s_k = -i\omega_0 c_k = e^{i\theta_k} - i\omega_0 r_k. \tag{4.10}$$

A circular relative equilibrium is obtained when all the centers coincide; this corresponds to the algebraic condition

$$P\mathbf{s} = 0, \quad P = I_N - \frac{1}{N}\mathbf{1}\mathbf{1}^\top. \tag{4.11}$$

This suggests to choose a stabilizing control that minimizes the Lyapunov function

$$S(\mathbf{r}, \theta) = \frac{1}{2}\|P\mathbf{s}\|^2. \tag{4.12}$$

Noting that

$$\dot{s}_k = ie^{i\theta_k}(u_k - \omega_0), \tag{4.13}$$

the time-derivative of S along the solutions of (4.1) is

$$\dot{S} =< P\mathbf{s}, P\dot{\mathbf{s}} >= \sum_{k=1}^{N} < P_k\mathbf{s}, ie^{i\theta_k} > (u_k - \omega_0) \tag{4.14}$$

where P_k denotes the k-th row of the matrix P and where we have used the fact that P is a projector, i.e. $P^2 = P$. Choosing the control law

$$u_k = \omega_0 - \kappa < P_k \mathbf{s}, ie^{i\theta_k} >, \quad \kappa > 0 \tag{4.15}$$

results in

$$\dot{S} = -\kappa \sum_{k=1}^{N} < P_k \mathbf{s}, ie^{i\theta_k} >^2 \leqslant 0. \tag{4.16}$$

Noting that

$$P_k \mathbf{s} = s_k - \frac{1}{N} \mathbf{1}^\top \mathbf{s} = e^{i\theta_k} - i\omega_0 r_k - (\dot{R} - i\omega_0 R), \tag{4.17}$$

we obtain

$$\begin{aligned} < P_k \mathbf{s}, ie^{i\theta_k} > &= - < \omega_0 (r_k - R), e^{i\theta_k} > - < \dot{R}, ie^{i\theta_k} > \\ &= - < \omega_0 \tilde{r}_k, e^{i\theta_k} > - \frac{\partial U_1}{\partial \theta_k} \end{aligned} \tag{4.18}$$

where we denote by $\tilde{r}_k = r_k - R$ the relative position of particle k from the group center of mass

$$R = \frac{1}{N} \sum_{k=1}^{N} r_k.$$

Using (4.18), we rewrite the control law (4.15) as

$$u_k = \kappa \frac{\partial U_1}{\partial \theta_k} + \omega_0 (1 + \kappa < \tilde{r}_k, \dot{r}_k >), \quad \kappa > 0, \ \omega_0 \neq 0. \tag{4.19}$$

Lyapunov analysis provides the following global convergence result given in [36].

Theorem 1: Consider the particle model (4.1) with the spacing control (4.15). All solutions converge to a relative equilibrium defined by a circular formation of radius $\rho_0 = |\omega_0|^{-1}$ with direction determined by the sign of $\omega_0 \neq 0$.

Proof: The Lyapunov function $S(\mathbf{r}, \theta)$ defined in (4.12) is positive definite and proper in the reduced shape space, that is, when all points $(\mathbf{r}, \theta)$ that differ only by a rigid translation $\mathbf{r}+\mathbf{1}r_0$ and a rigid rotation $\theta+\mathbf{1}\theta_0$ are identified. From (4.16), S is nonincreasing along the solutions and, by the LaSalle Invariance principle, solutions for the reduced system on shape space converge to the largest invariant set Λ where

$$\kappa < P_k\mathbf{s}, ie^{i\theta_k} > \equiv 0 \tag{4.20}$$

for $k = 1, \ldots N$. In this set, $\dot{\theta}_k = \omega_0$ and s_k is constant for all $k = 1, \ldots N$. This means that (4.20) can hold only if $P\mathbf{s} \equiv 0$. As a result, $\mathbf{s} = \mathbf{1}s_0$ for some fixed $s_0 \in \mathbb{C}$, i.e., all particles orbit the same circle of radius ρ_0. ■

A slightly more sophisticated version of the analysis allows for coordinated control to shapes that don't necessarily share the same center [31].

4.3 Resonance Patterns

As set out in Section 4.1, we present an adaptation of the control laws developed for single-beat patterns to resonance formations, focussing on the heading (phase) component. The form of the control and the stability proof mirrors that of the single beat pattern control presented in detail in [36]. A logical extension of the work presented in this thesis would be the controls for limited communication conditions similar to those presented in [37] for single-beat patterns.

4.3.1 Phase control for Resonance Patterns

Consider N particles moving at constant speed. Let

$$\alpha_k \in \mathbb{N}, \quad k = 1, \ldots, N \tag{4.21}$$

and

$$\alpha_o = \max_k \alpha_k$$

be scalar coefficients determining the order of the resonance in phase coordinates. For example, for the two particles in Figure 4.1 $\alpha_1 = 1, \alpha_2 = \alpha_0 = 2$, resulting in a **1-2** resonance formation. We desire the particle k to move around a circle of radius $\frac{\alpha_k}{|\omega_o|\alpha_o}$. In this case, the particle would be rotating with frequency $\omega_k = \frac{\omega_o \alpha_o}{\alpha_k}$ where positive values of ω_k correspond to counterclockwise rotation. We consider the phase dynamics:

$$\alpha_k \dot{\theta}_k = \alpha_o \omega_o + K \sum_{j=1}^{N} \sin\left(\alpha_k \theta_k - \alpha_j \theta_j\right), \quad k = 1, \ldots, N \tag{4.22}$$

where K is a scalar gain. From a rotating frame at $\alpha_o \omega_o$ this becomes

$$\alpha_k \dot{\theta}_k = K \sum_{j=1}^{N} \sin\left(\alpha_k \theta_k - \alpha_j \theta_j\right). \tag{4.23}$$

Introducing a change of coordinates $\phi_k = \alpha_k \theta_k$, (4.23) becomes

$$\dot{\phi}_k = K \sum_{j=1}^{N} \sin\left(\phi_j - \phi_k\right) \tag{4.24}$$

which are gradient dynamics where

$$\dot{\phi}_k = \frac{\partial U}{\partial \phi_k} = \alpha_k \dot{\theta}_k, \tag{4.25}$$

$$U = \frac{N}{2}|p(\boldsymbol{\alpha\theta})|^2 = \frac{N}{2}|p(\boldsymbol{\phi})|^2 \tag{4.26}$$

and

$$p(\boldsymbol{\phi}) = \frac{1}{N}\sum_{k=1}^{N} e^{i\phi_k} = \frac{1}{N}\sum_{k=1}^{N} e^{i\alpha_k\theta_k} = p(\boldsymbol{\alpha\theta}), \tag{4.27}$$

where $\boldsymbol{\alpha\theta} = (\alpha_1\theta_1, \ldots, \alpha_N\theta_N)^\top$.

From (4.24),(4.25) and (4.6) the control law becomes for $k = 1, \ldots, N$

$$\dot{\theta}_k = u_k = \frac{1}{\alpha_k}\dot{\phi}_k = -\frac{1}{\alpha_k}K < ie^{i\boldsymbol{\phi}}, p(\boldsymbol{\phi}) >= \frac{1}{\alpha_k}K\sum_{k=1}^{N}\sin\left(\alpha_k\theta_k - \alpha_j\theta_j\right), \tag{4.28}$$

and the expression for $\dot{U}$ becomes

$$\dot{U} = -K\sum_{k=1}^{N} < p(\boldsymbol{\phi}), ie^{i\phi_k} >^2 \leqslant 0. \tag{4.29}$$

If the inequality in (4.29) were strict, that would be the end of the stability proof. Since $\dot{U}$ is *less or equal* than zero, we must consider the case when $< p(\boldsymbol{\phi}), ie^{i\phi_k} >= 0$. Notably, this problem has been studied by Sepulchre, Paley and Leonard and presented in [36] and other papers on that topic. Therefore, the theorem below from [36] directly applies to the present problem and is presented here merely for completeness of the argument. The important feature of the resonance patterns that is apparent from what we have shown above is that control for resonance patterns is *compatible* with that for single-beat patterns extensively studied by others. This makes it possible to use resonance patterns in ways that compliment the existing methods and, in light of Chapter 3, enhance the performance of the sampling array.

One difference as compared to the control law for single-beat patterns is that for resonance patterns control no longer depends only on relative phases θ_{jk}, but instead on measurements of the form $\phi_j - \phi_k = \alpha_j\theta_j - \alpha_k\theta_k$. This difference has

some implications on the design of a sensor network from a practical engineering standpoint. Consider a mobile sensor network design where vehicles are capable of measuring the relative phase θ_{jk} between themselves and other vehicles. If in the case of single-beat patterns this was enough to determine the control effort, this information is no longer sufficient for resonance tracks. In addition we need to know α_j, α_k, and the k'th vehicle would have to know its own absolute angle θ_k to determine the 'relative phase' in its new meaning.

The following theorem and proof is taken from [36].

Theorem 2: The potential $U = \frac{N}{2}|p(\boldsymbol{\phi})|^2$ reaches its unique minimum when $p(\boldsymbol{\phi}) = 0$ (balancing) and its unique maximum when all phases are identical (synchronization). All other critical points of U are isolated in the shape manifold $\mathbb{T}^N/\mathbb{S}^1$ and are saddle points of U. The phase model $\dot{\theta}_k = u_k$ with the gradient control (4.28) forces convergence of all solutions to the critical set of U. If $K < 0$, then only the set of synchronized states is asymptotically stable and every other equilibrium is unstable. If $K > 0$, then only the balanced set where $p(\boldsymbol{\phi}) = 0$ is asymptotically stable and every other equilibrium is unstable.

Proof: The gradient dynamics $\dot{\phi}_k = \frac{\partial U}{\partial \phi_k}$ forces convergence of all solutions to the set of critical points of U, characterized by the N algebraic equations

$$< p(\boldsymbol{\phi}), ie^{i\phi_k} >= 0, \quad k = 1, \ldots, N. \tag{4.30}$$

Critical points where $p(\boldsymbol{\phi}) = 0$ are global minima of U. As a consequence, the balanced set is asymptotically stable if $K > 0$ and unstable if $K < 0$. From (4.30), critical points where $p(\boldsymbol{\phi}) \triangleq |p(\boldsymbol{\phi})|e^{i\Psi} \neq 0$ are characterized by $\sin(p(\boldsymbol{\phi}) - \Psi) = 0$, that is, $N - M$ phases synchronized at $\Psi \mod 2\pi$ and M phases synchronized at $(\Psi + \pi) \mod 2\pi$, with $0 \leqslant M < \frac{N}{2}$. At those points, $|p(\boldsymbol{\phi})| = 1 - \frac{2M}{N} > \frac{1}{N}$. The value $M = 0$ defines a synchronized state and corre-

sponds to a global maximum of U. As a consequence, the set of synchronized states is asymptotically stable if $K < 0$ and unstable if $K > 0$.

Every other value $1 \leqslant M < \frac{N}{2}$. corresponds to a saddle and is therefore unstable both for $K > 0$ and $K < 0$. This is because the second derivative

$$\frac{\partial^2 U}{\partial {\phi_k}^2} = \frac{1}{N} - < p(\boldsymbol{\phi}), ie^{i\phi_k} >= \frac{1}{N} - \cos\Psi - \phi_k |p(\boldsymbol{\phi})| \tag{4.31}$$

takes negative values if $\phi_k = \Psi$ and positive values if $\phi_k = \Psi + \pi$. As a consequence, a small variation $\delta\phi_k$ at those critical points decreases the value of U if $\phi_k = \Psi$ and increases the value of U if $\phi_k = \Psi + \pi$. ■

4.3.2 Control to Resonance Patterns in Simulation

We illustrate by simulation the phase control law (4.28) developed in Section 4.3.1 in conjunction with the spacing controls presented in [31] for $N = 2$ particles, and the gain $K = -0.5$. The sequence of representative frames show convergence of the two particles starting from random initial conditions to a specified configuration (both shape and relative phase). The desired tracks were given as two circular paths with $R_2 = \frac{1}{2}R_1$ where R_1 and R_2 are the radii of the tracks, and the center of smaller circle offset upward by R_2 from the center of the larger circle to illustrate synchronization. Note that in Frame 9, a **1-2** resonance is achieved with two gliders in phase. Recall from Chapter 3 that in a **1-2** resonance pattern, the perimeter of the larger track is twice the perimeter of the smaller track, which allows for a phase synchronization such that the two particles meet at the top of their tracks every other revolution of the particle on the smaller track.

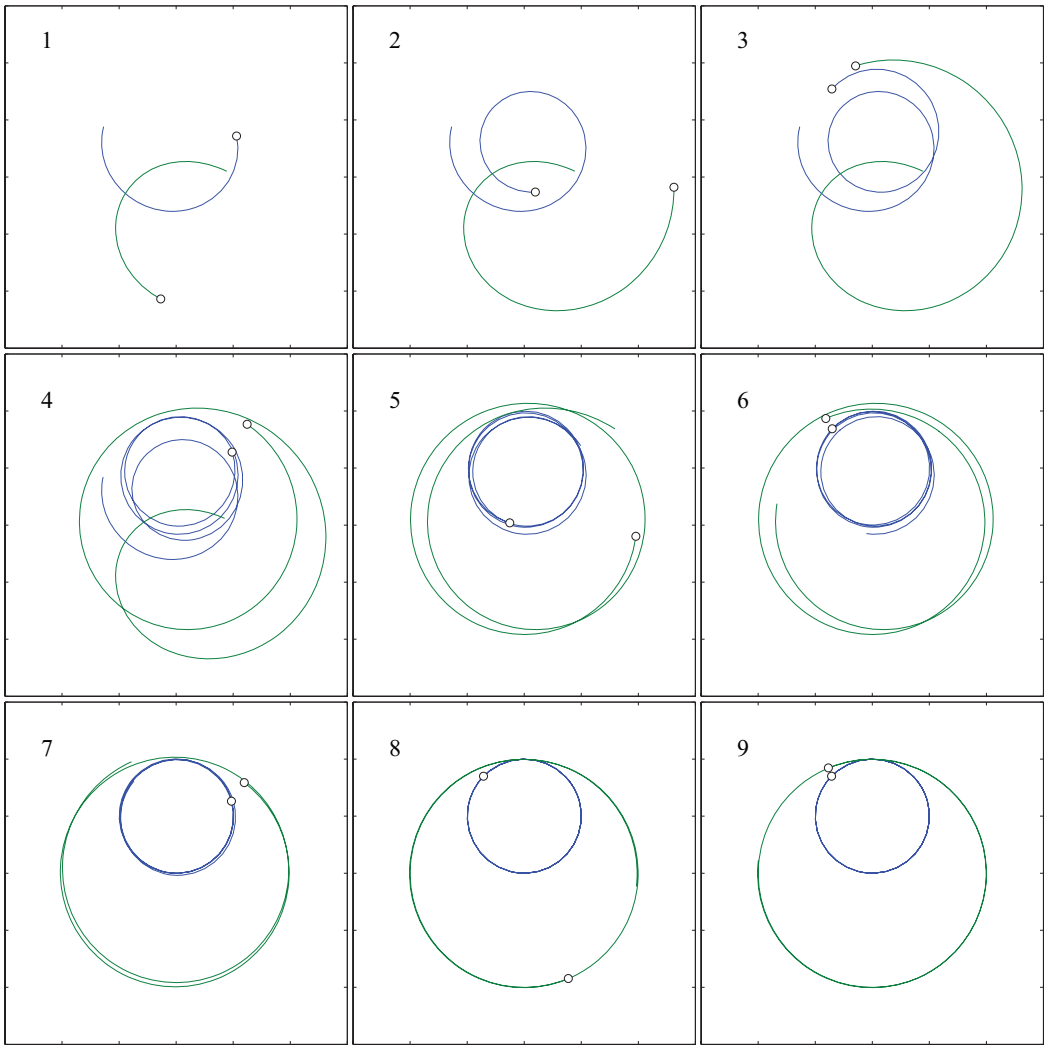

Figure 4.1: Representative frames illustrating the performance of the phase control for **1-2** resonance formation in conjunction with the spacing (shape) control developed in [31] for single-beat patterns. Two particles start from random initial conditions in Frame 1 and are controlled to the final configuration achieved in Frame 9 circling the respective tracks in counter-clockwise direction. The frames illustrate last 200 time steps of the particle motion, and small circles denote the final position of the particle in snap shot.

Chapter 5

Conclusions and Future Work

5.1 Conclusions

The core value of the work presented in this thesis is in providing guidelines on how to use multiple vehicles for collecting the data. In Chapter 1, we gave a general overview of the coverage problem, identified relevant theoretical frameworks, and focussed our development on application of this work to Autonomous Underwater Vehicles (AUVs) in the context of ocean exploration. In Chapter 2 we reviewed the methods of Objective Analysis (OA), and described a new fast metric evaluation scheme that is used in Chapter 3 as a measure of richness of data collected on a given sampling trajectory. We performed a numerical optimization study to identify trajectories that have the best performance in various environments characterized by spatial and temporal scales. In Chapter 4 we reviewed the control laws presented in [36] and [31] and extended those results in Section 4.3.1 to achieve phase control of resonance patterns.

5.1.1 Objective Analysis

The derivation in Section 2.1 showed that the matrix $\mathbf{A}$ given by

$$\mathbf{A} = \mathbf{B} - \mathbf{B}\mathbf{H}^\top(\mathbf{W} + \mathbf{H}\mathbf{B}\mathbf{H}^\top)^{-1}\mathbf{B}$$

with the appropriate norm

$$\|\mathbf{A}\| = \frac{1}{\dim(\mathbf{A})}\mathrm{Tr}(\mathbf{A})$$

can be used as a metric for evaluating the performance of sampling patterns. This result has been known since it was first developed by Eliassen et al [12] in 1954 and later independently reproduced and popularized by Gandin [13] in 1963. This method however involves a large matrix inversion, which even with the current-day powerful computing systems take significant computation time. This limitation makes this method impractical for metric-driven optimization of sampling tracks since we rely on evaluations of the metric for each optimization step.

We then proceeded in Section 2.2, following [21], to describe equations similar to those in Section 2.1 in continuous space, which with reasonable assumptions about the domain and the form of covariance function, allowed us to express $\|\mathbf{A}\|$ in a 'computationally friendly' way:

$$\begin{aligned}\|\mathbf{A}\| \quad = \quad & \sum_{ij} \Psi^{-1}(\mathbf{z}_i^m, \mathbf{z}_j^m)\; e^{-\frac{(x_i^m - x_j^m)^2}{2\sigma^2} - \frac{(y_i^m - y_j^m)^2}{2\sigma^2} - \frac{(t_i^m - t_j^m)^2}{2\tau^2}} \\ & \times \int_{-D_x}^{D_x} dx\; e^{-\frac{\left(x - \frac{x_i^m + x_j^m}{2}\right)^2}{(\sigma/\sqrt{2})^2}} \int_{-D_y}^{D_y} dy\; e^{-\frac{\left(y - \frac{y_i^m + y_j^m}{2}\right)^2}{(\sigma/\sqrt{2})^2}} \int_{-D_t}^{D_t} dt\; e^{-\frac{\left(t - \frac{t_i^m + t_j^m}{2}\right)^2}{(\tau/\sqrt{2})^2}}.\end{aligned}$$

The integrals above are solved analytically yielding an expression involving error functions erf$(\cdot)$, which are easily (and quickly) computed using built-in function in MATLAB.

5.1.2 Track Design

In Chapter 3 we took on the task of designing the tracks that would best suit the needs of a sampling experiment. The goal was identified as collecting the richest data set given four gliders moving at uniform speed in a simple domain. The measure of "richness of data set" was provided by the OA metric developed in the previous chapter. We made the choice to focus on *structured sampling patterns* - parameterizable and repeatable elliptical tracks. We also gave references to alternative approaches to sampling using mobile sensor networks that have been studied in the past. To validate our approach we quantitatively compared it to the 'lawn mower patterns' that have been traditionally used for sampling.

We implemented a modified steepest ascent algorithm to find patterns that produce the richest data set (largest value of the OA metric) as a function of oceanographic parameters $S\mathfrak{z}$ and $S\mathfrak{t}$ incorporating spatial and temporal decorrelation scales. Noticing certain trends in resulting patterns, we limited the parameter set to channel the computational resources to finding the best patterns as a function of region of $(S\mathfrak{z}, S\mathfrak{t})$ space. The results of pattern optimization are presented in Figure 3.9 and the corresponding subsets of parameter space $(S\mathfrak{z}, S\mathfrak{t})$ are identified in Figure 3.10.

5.1.3 Controls

In Chapter 4 we considered control laws necessary to stabilize the vehicles to the tracks designed in Chapter 3. We used the *particle model* that has appeared

earlier in numerous publications such as [31], [18], and [23] to name a few:

$$\begin{aligned} \dot{r}_k &= e^{i\theta_k} \\ \dot{\theta}_k &= u_k, \quad k = 1, \ldots, N. \end{aligned}$$

The control input u_k is the rate of change of heading of each vehicle. We assume that the vehicles move with uniform speed, and control can be interpreted as a steering control.

The controls are the sum of spacing (shape) and phase controls. The former ensures that vehicles follow a track of appropriate shape, while the latter puts the vehicles into a desired relative phase arrangement:

$$u_k = \omega_0 + u_k^{spac}(\mathbf{r}, \boldsymbol{\theta}) + u_k^{phase}(\boldsymbol{\theta}), \quad \omega_0 \in \mathbb{R}, \quad k = 1, \ldots, N.$$

Following [36] and [31] we reviewed the control laws for single-beat patterns. Then, focussing on the *phase* portion of the control, we extended those results to cases involving resonance patterns. Remarkably, the derivation of control laws for phase resonance followed similar steps as in [36], which made controls for single-beat patterns a *special case* of the resonance (with all α equal). Consequently, this new approach can be viewed as a *generalization* of the previous work that adds more capabilities to the sampling array rather than a new paradigm that will require restructuring of existing frameworks. One difference as compared to the control law for single-beat patterns is that for resonance patterns control no longer depends only on relative phases θ_{jk}, but instead on measurements of the form $\phi_j - \phi_k = \alpha_j\theta_j - \alpha_k\theta_k$.

Finally, we simulated the vehicle motion with resonance control and demonstrated in Figure 4.1 the convergence to desired phase configuration.

5.2 Future Work

5.2.1 Robustness Analysis

A whole set of limitations of the work presented in this thesis arises from the fact that we do not take into account *currents and other disturbances*. Velocity of the currents can sometimes be as large in magnitude as the that of the gliders [35]. This can increase or decrease a glider's effective speed and push the gliders off their tracks. In fact, during the experiments in Monterey Bay (see Section 1.3.2) there were occasions when gliders were driven so far off the tracks by the strong currents that the entire design of the sampling trajectories had to be adjusted to account for such disturbances.

Given our ability to separate the coverage problem into track design and track control subproblems, we have an option of dealing with currents separately for each subproblem. Consider the track design. One way to introduce currents would be to simply simulate the motion of the gliders under a specified flow field using the existing control laws. This would provide positions of the measurement points which can be used to evaluate sensor array performance in that configuration under the specified flow conditions. This approach, however, has a number of limitations. For instance, it requires a fairly accurate knowledge of the currents, which is not always the case, especially if there were no previous experiments in that domain, or the goal of the experiment is to collect data about currents. If the anticipated currents differ from reality by a large margin, the pattern would not be optimal for this environment, and we would not gain much with this added complexity over the original no-flow approach. The second important limitation is that this approach requires that

we run the glider simulator on every step of the optimization, which increases computational time to the point when it becomes impractical.

From the track optimization point of view, it is irrelevant how the list of measuring sites was generated – by a low-level spacing routine directly on the tracks (as considered in this thesis), or by a sophisticated glider simulator with currents and disturbances, or by any other means. If one could come up with a clever (and fast) way to generate the list of measuring sites that would take into account effects of currents, this would eliminate the issue with computation time. However, this would not do much good unless we have an estimate of the trends of the currents. Therefore, it might be more useful to think of the currents issue in terms of *robustness analysis.*

Instead of computing the performance of a pattern just when the gliders stay exactly on tracks, one can characterize patterns for a neighborhood of tracks. That way we can gain insight into how a particular configuration will perform if the gliders get pushed off tracks slightly or they are unable to coordinate relative phases as required. It may happen that performance of a pattern with no disturbances would be significantly diminished if the gliders were blown off track by the currents, while a good but not the best pattern may stay good even under disturbances. Consider Figure 5.1 where we sketched the 'bandwidth of performance' of three hypothetical patterns. A pattern corresponding to Panel A performs very well, but for a small family of curves near the optimal one. This means that if the gliders are forced off the optimal track, the performance of the array will decrease dramatically. A pattern corresponding to the performance curve in Panel B, on the other hand, is not as good as A on the peak, but it is more robust to the disturbances. Similarly, Panel C depicts a case with mediocre peak performance, but large 'margin of error'. This kind of information would be useful to a scientist planning an experiment. She would have an option to

choose among candidate patterns that either provide high performance or high flexibility, or somewhere in between.

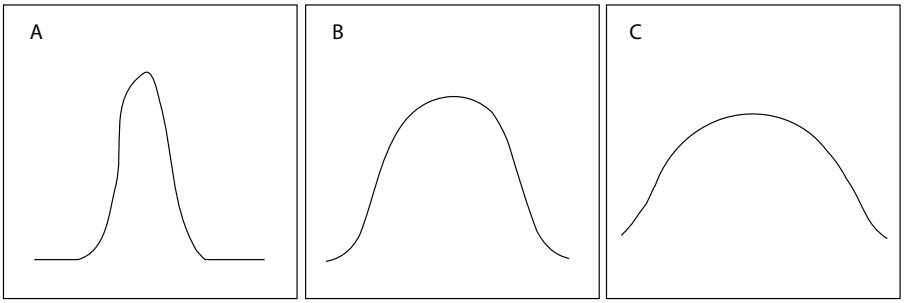

Figure 5.1: The bandwidth of optimal performance. Tracks can be characterized not only by their peak performance when the gliders stay exactly on tracks, but also how they perform if the gliders are a little bit off.

5.2.2 Transient Performance and Control

Often in the real experiment it is infeasible or impractical to deploy the gliders (or other mobile sensors) in the exact spot where they need to be to start collecting data in formation. Usually the vehicles are deployed from one spot and then 'driven' to their designated locations, after which the controls do their job of keeping them on tracks. They are typically collecting data while getting to their respective spots. It takes time and resources to do that, and there might be an efficient way to get the gliders to their designated positions so that they collect useful data while enroute. One can design a *transient pattern* with associated controls, and optimize it using the methods similar to those described in this thesis. That way the experiment starts from the minute the vehicles are released and the useful data (perhaps pertaining to the costal areas if the vehicles are released form near the shore) is generated while they are moving to where they eventually need to be.

5.2.3 Improvements to Resonance Control Law

In Chapter 4 we develop a control law for phase synchronization of resonance patterns that parallels the development in [36] for single-beat patterns with *all-to-all communication.* The next step would be to consider the the case with *limited communication* as presented in [37] for single-beat patterns, and extend those results to allow synchronization for resonance patterns. Also, one could extend the results of Section 4.3.1 to include control of the resonance patterns to elliptical/superelliptical shapes following the work in [31].

5.2.4 Lawn Mower Patterns

The idea of using *lawn mower patterns* to collect data as described in Section 3.3 is not a bad one and may, for certain applications, lead to interesting results. It was shown in Figure 3.7 that the performance of such patterns are in general not as good as that of the symmetric patterns. However, if the scientific interest provides substantial incentives to collect data on straight lines and we have few mobile sensors to work with, a properly optimized lawn mower pattern could be a good option.

The approach that we took in this thesis with regards to *how* multiple gliders follow a lawn mower pattern is admittedly a simplistic one. We assumed that the gliders were separated by a static 'rod' of length d pivoted at the center and rotated the angle θ form horizontal, so that the center point follows the lawn mower pattern (see Figure 3.6 for illustration). One could explore the possibilities of using the ideas of 'virtual leaders' (as describes for example in [22] and references therein) to enhance the performance of lawn mower patterns. A point on the lawn mover track moving at some speed (perhaps dynamically controlled) would be the virtual leader that the real gliders would follow.

Further, one can develop a 'dynamic rod' approach where d and θ are allowed to change dynamically using feedback from the position of the vehicles on a lawn mower track. There might be some interesting dynamics as the vehicles curve around the corners of the lawn mower sweeps: sharp edges are somewhat unnatural for the optimized glider motion and a dynamic rod could be a good way to smooth them out. Note that by saying 'rod' we do not imply that we only consider this pattern for two-vehicle formation. The 'rod' can become a 'Y' or a 'cross' when more vehicles are involved. This possibility can be realized using the virtual bodies approach of [29].

5.2.5 Gain Parameters

As we mentioned in Chapter 3, control laws used to control the gliders in Monterey Bay experiments [35] such as developed in [31], [36] and [37], consist of two parts: phase control that is responsible for keeping gliders in a desired relative phase configuration and spacing control that drives the gliders to their respective tracks. Each of those components has a *scalar gain parameter* that determines how strongly the individual vehicles are affected by each control term. In some sense, this sets the priorities of the control effort. For example, if the gain on spacing control is set higher than on phase control, the gliders would be strongly driven to their tracks, and as a second priority, the phase control will try to distribute the vehicles according to their prescribed phase arrangement.

Currents in a real ocean experiment such as the one performed in Monterey Bay (see Section 1.1.2) could be as large as the still-water speed of the gliders [35]. This means that if the gliders are opposing the current and the gains on control are set high, the gliders will make little or no progress forward. This of

course is detrimental to the performance because during that time the gliders are collecting redundant data. In those circumstances, decisions have to be made as to how best to compromise between staying on track and making headway along the path. Such a trade-off can be accomplished by lowering the gains on the controls and allowing the gliders to be pushed off the tracks. At this point, this is a human-in-the-loop operation that requires presence and attention of scientists. It would be a significant contribution to the field to have an algorithm to dynamically adapt control gains so that the overall performance of the sensor array is optimized.

Controlling the gains on control effort is also important from the oceanographic point of view. In an ocean environment such as Monterey Bay, the temperature gradients are likely to be associated with velocity gradients. Cutting through such gradients is likely to be the preferred strategy (for scientific purposes), rather than simply trying to run the gliders up current. Relaxing the gains in an optimal way would allow the gliders to collect more valuable oceanographic data as well as avoiding the hinderance of the strong currents.

Appendix A

Two- and Three-Glider Formations

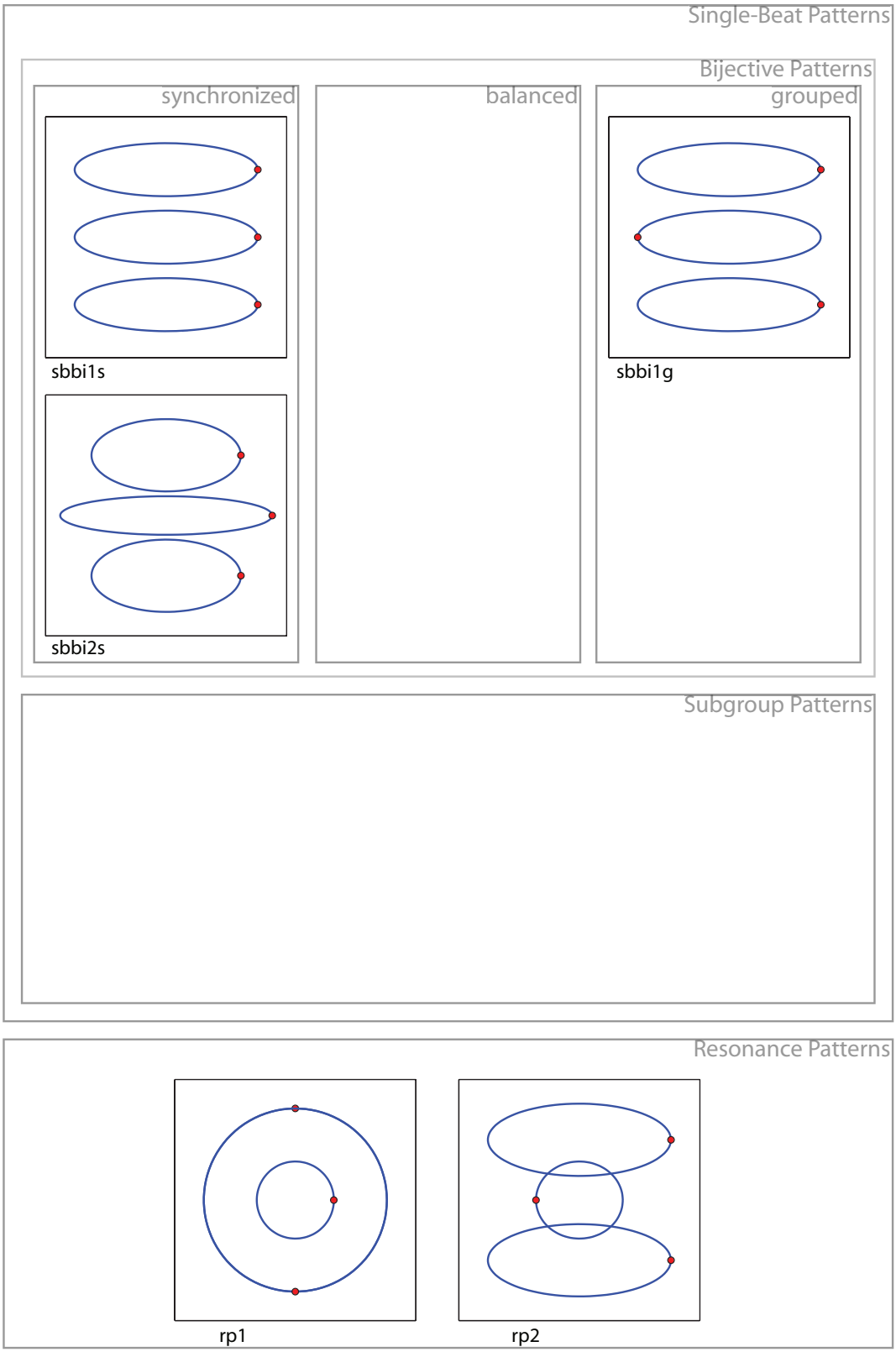

Figure A.1: Classification of optimized symmetric Three-Glider patterns.

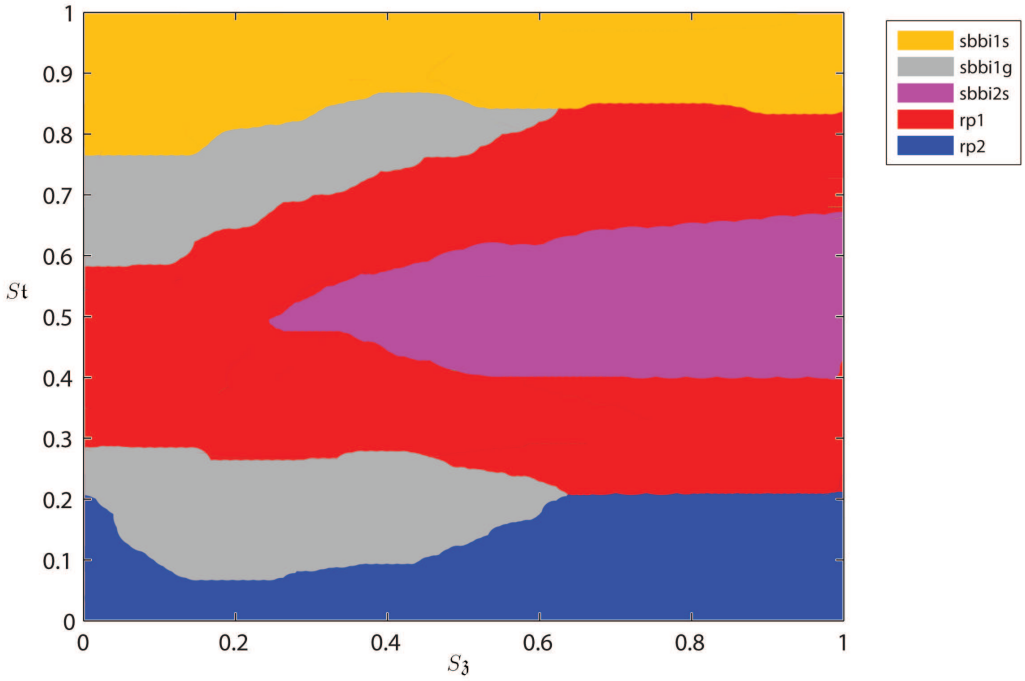

Figure A.2: Best patterns on the grid of parameters $S\mathfrak{z}$ and $S\mathfrak{t}$ for Three-Glider formations corresponding to the patterns classified in Figure A.1.

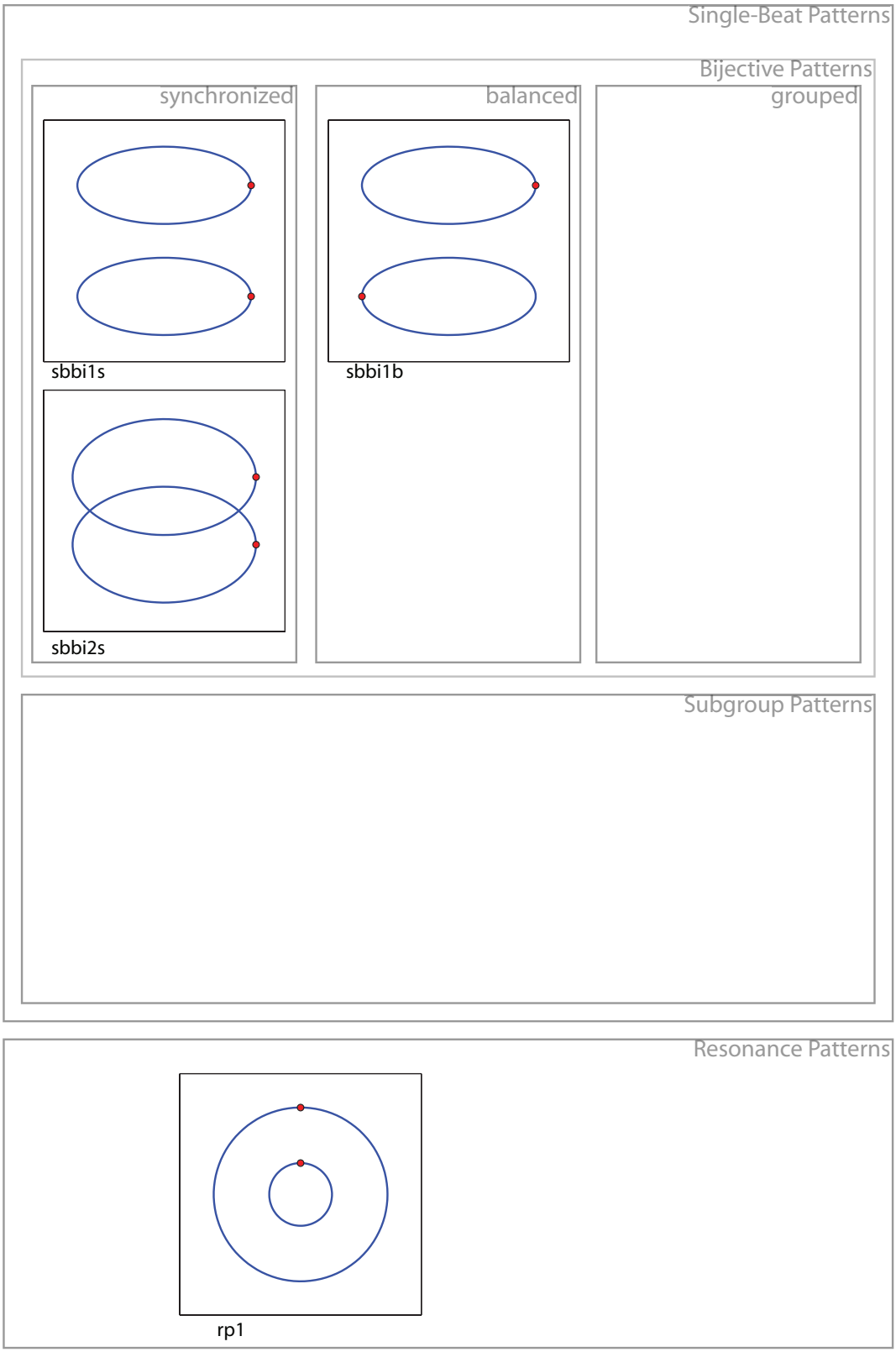

Figure A.3: Classification of optimized symmetric Two-Glider patterns.

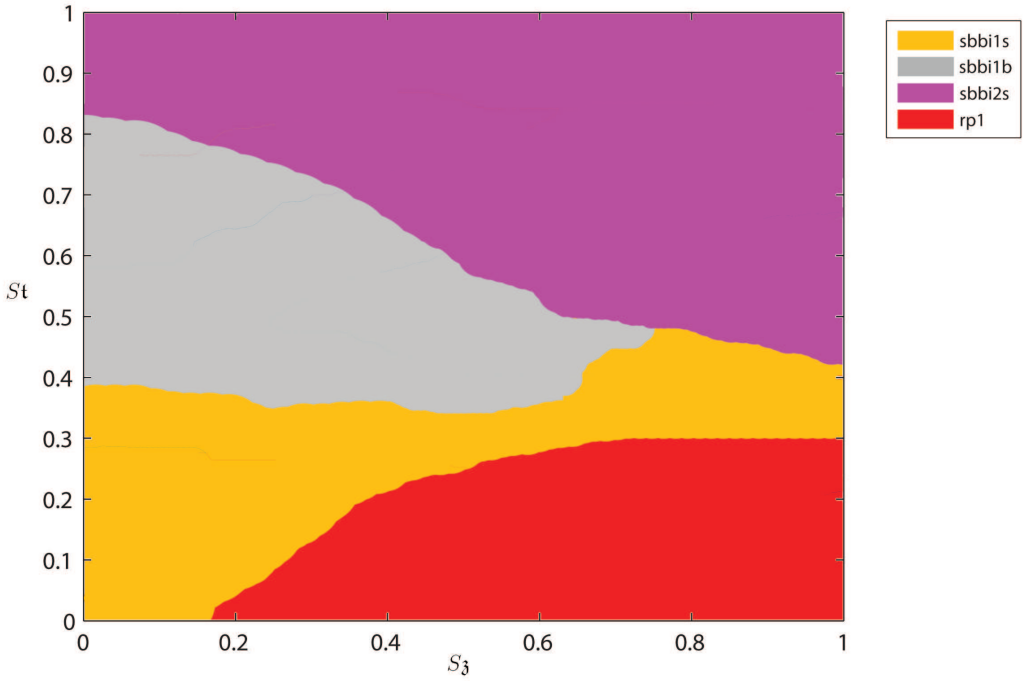

Figure A.4: Best patterns on the grid of parameters $S\mathfrak{z}$ and $S\mathfrak{t}$ for Two-Glider formations corresponding to the patterns classified in Figure A.3.

Appendix B

Numerical Results of Pattern Optimization

The figures below show the numerical results parameters for optimal patterns

gl(n).a semimajor axis of the elliptical track

gl(n).b semimajor axis of the elliptical track

gl(n).cx x-coordinate of the track

gl(n).cy y-coordinate of the track

gl(n).phase phase of the n-th glider[1]

where n is the identification number of the glider. The values are given on the $x \in [-50, 50],\ y \in [-50, 50]$ square domain with gl(n).phase $= 0$ corresponding to the positive x direction. Note that those values would change slightly when computed for *exact* values of $(S\mathfrak{z}, S\mathfrak{t})$. The values presented here correspond to the values on the grid points on which the optimization was performed (see

[1]Recall that only the *relative* phase is important. The parameter gl(n).phase should not be considered as fixed, but rather in relation to phases of other gliders in that pattern.

Section 3.2 for details). Also note that the numerical values of the metric would change slightly if we are not precisely on the grid point. In general, patterns were determined to be optimal on subsets of parameter space $(S\mathfrak{z}, S\mathfrak{t})$ by comparing the OA metric values of all candidate patterns. The OA metric values differ from grid point to grid point, and we do not display the values here since the patterns are found to be optimal over *many* grid points. Optimization results are displayed for each pattern such that they overlay the faint picture of the corresponding track on the background.

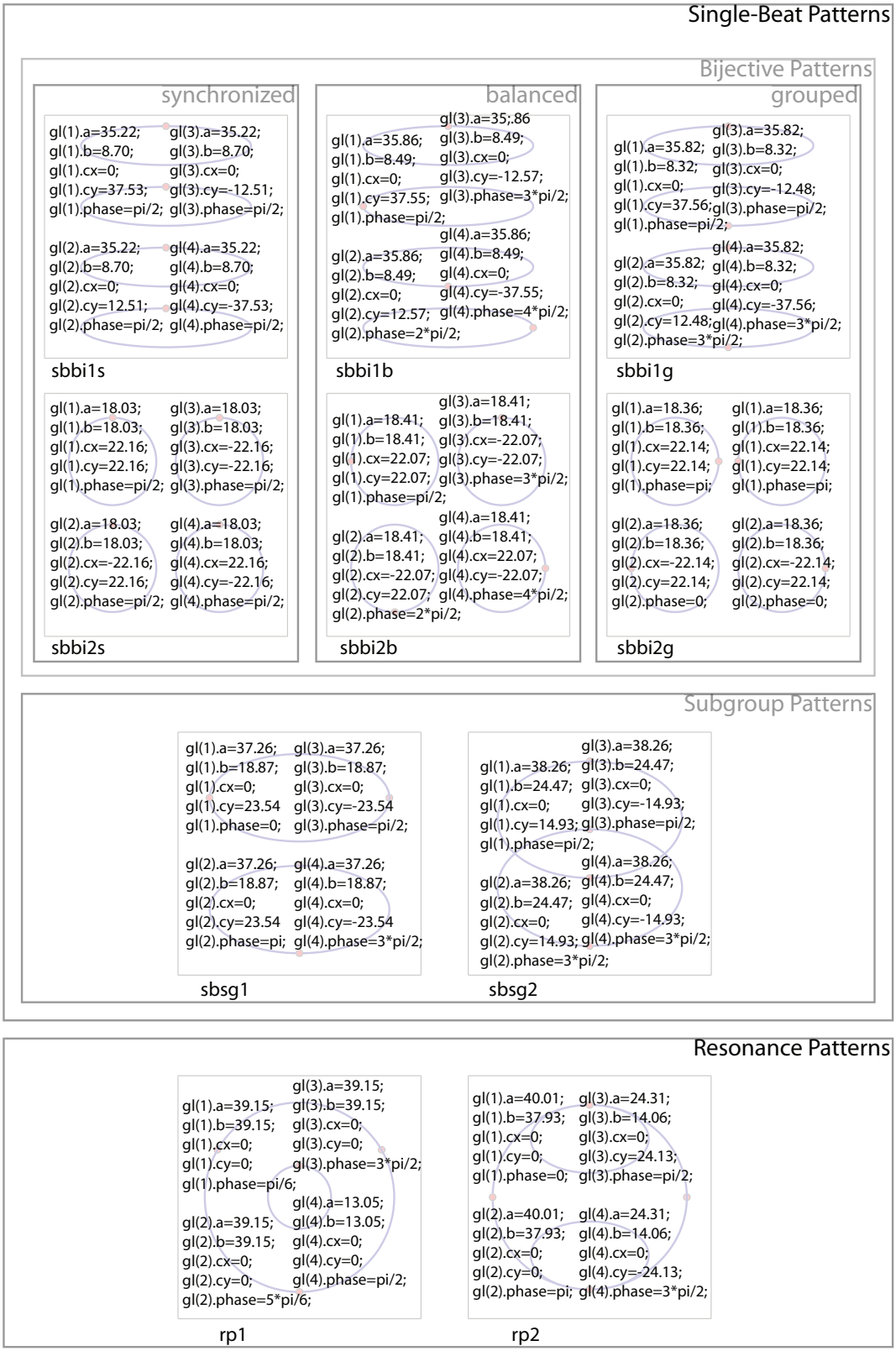

Figure B.1: Numerical results for optimized patterns (Four-Glider formations)

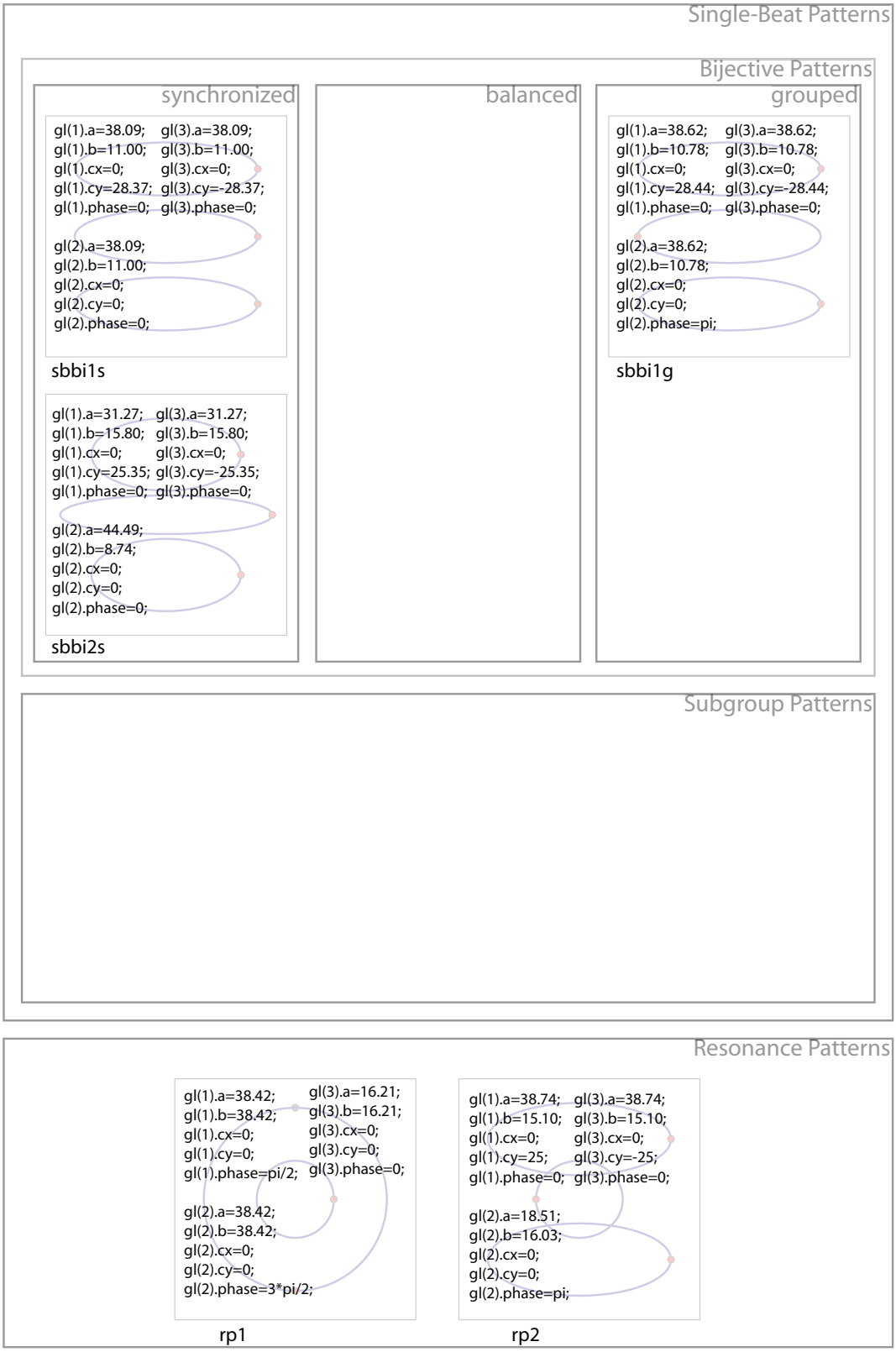

Figure B.2: Numerical results for optimized patterns (Three-Glider formations)

Figure B.3: Numerical results for optimized patterns (Two-Glider formations)

Bibliography

[1] *Adaptive Sampling and Prediction (ASAP).* http://www.princeton.edu/ dcsl/asap/, accessed May 2007.

[2] E. Ana, M. R. Dhanaka, L. K. Shayb, S. Smith, and J. Van Lee. Coastal oceanography using a small AUV. *Journal of Atmospheric and Oceanic Technology*, 18, February 2001.

[3] A. Bennett. *Inverse modeling of the ocean and atmosphere.* Cambridge: Cambridge University Press, 2002.

[4] A. F. Bennetta, B. S. Chuaa, D. E. Harrisonb, and M. J. McPhaden. Generalized inversion of tropical atmosphereocean data and a coupled model of the tropical pacific. *American Meteorological Sociaty: Journal of Climate*, 11:1768–1792, 1998.

[5] F. P. Bretherton, R. E. Davis, and C. B. Fandry. A technique for objective analysis and design of oceanographic experiments applied to mode-73. *Deep-Sea Research*, 23:559–582, 1976.

[6] T. Clarke. Oceanography: Robots in the deep. *Nature*, 421:468–470, January 2003.

[7] D. Van Cleave. *Trends and technologies for uninhabited autonomous vehicles. In Software-Enabled Control: Information Technology for Dynamical Systems*. IEEE Press/John Wiley and Sons, 2002.

[8] J. Cortès and F. Bullo. Coordination and geometric optimization via distributed dynamical systems. *SIAM J. Control Optim.*, 44(5):1543–1574, 2005.

[9] J. Cortès, S. Martìnez, T. Karatas, and F. Bullo. Coverage control for mobile sensing networks. *IEEE Transactions on Robotics and Automation*, 20(2):243–255, 2004.

[10] R. D'Andrea. Robot soccer: a platform for systems engineering. *Computers in Education Journal*, 10:57–61, 2000.

[11] T. Delcroixa, M. J. McPhadenb, A. Dessierc, and Y. Gouriou. Time and space scales for sea surface salinity in the tropical oceans. *Deep-Sea Research I*, 52:787–813, 2005.

[12] A. Eliassen, J. S. Sawyer, and J. Smagorinsky. Upper air network requirements for numerical weather prediction. *Technical Note of the World Meteorological Organization*, 29, 1954.

[13] L. S. Gandin. *Gidrometerologicheskoe Izdatelstvo Objective Analysis of Meteorological Fields*. Leningrad, Jerusalem: English Translation by Israeli Program for Scientific Translations, 1963.

[14] VOCALS Scientific Working Group. *VAMOS Ocean-Cloud-Atmosphere-Land Study (VOCALS)*. Available: http://www.atmos.washington.edu/ breth/VOCALS/VOCALS-Implementation-Plan.pdf, 2005.

[15] P. Hall. *Introduction to the theory of coverage processes.* New York, John Wiley and Sons, 1988.

[16] Y. Kuramoto in: H. Arakai (Ed.). International symposium on mathematical problems in theoretical physics. *Lecture Notes in Physics*, 39:420, 1975.

[17] D. S. Battisti J. J. Barsugli. The basic effects of atmosphereocean thermal coupling on midlatitude variability. *Journal of the Atmospheric Sciences*, 55:477–493, 1998.

[18] E. W. Justh and P. S. Krishnaprasad. Equilibria and steering laws for planar formations. *Systems and Control Letters*, 52:25–38, 2004.

[19] E. Kalnay. *Atmospheric modeling, data assimilation, and Predictability.* Cambridge: Cambridge University Press, 2003.

[20] Y. Kuramoto. *Chemical Oscillations, Waves, and Turbulence.* Springer, Berlin, 1984.

[21] F. Lekien, R. E. Davis, and N. E. Leonard. Sampling performances and optimization in Monterey Bay. *International Journal for Numerical Methods in Engineering*, [Submitted] 2007.

[22] N. E. Leonard and E. Fiorelli. Virtual leaders, artificial potentials and coordinated control of groups. *Proc. 40th IEEE Conf. Decision and Control*, pages 2968 – 2973, 2001.

[23] N. E. Leonard, D. A. Paley, F. Lekien, R. Sepulchre, D. M. Fratantoni, and R. E. Davis. Collective motion, sensor networks and ocean sampling. *Proceedings of the IEEE*, 95(1):48–74, 2007.

[24] P. F. J. Lermusiaux. Uncertainty estimation and prediction for the interdisciplinary ocean. *J. Comp. Phys.*, 2005.

[25] P. F. J. Lermusiaux, C. S. Chiu, G. C. Gawarkiev, P. Abbot, A. R. Robinson, P. J. Haley, P. J. Leslie, S. J. Majumdar, A. Pang, and F. Lekien. Quantifying uncertainties in ocean predictions. *Oceanography*, 19:80–93, 2006.

[26] W. Li and C. G. Cassandras. Distributed cooperative coverage control of sensor networks. *Proc. 44th IEEE Conf. Decision and Control*, pages 2542–2547, 2005.

[27] H. Malchow, B. Radtke, M. Kallache, A. B. Medvinsky, D. A. Tikhonov, and S. V. Petrovskii. Spatio-temporal pattern formation in coupled models of plankton dynamics and fish school motion. *Nonlinear Analysis: Real World Applications*, 1:53–67, March 2000.

[28] N. Muscettola, P. Pandurang Nayak, B. Pell, and B.C. Williams. Remote agent: To boldly go where no AI system has gone before. *Artificial Intelligence*, 103:5–48, 1998.

[29] P Ögren, E. Fiorelli, and N. E. Leonard. Cooperative control of mobile sensor networks: Adaptive gradient climbing in a distributed environment. *IEEE Transactions on Automatic Control*, 49:8:1292–1302, August 2004.

[30] D. A. Paley. *Cooperative Control of Collective Motion and Ocean Sampling with Autonomous Vehicles.* PhD thesis, Princeton University, 2007. in preparation.

[31] D. A. Paley, N. E. Leonard, and R. Sepulchre. Collective motion of self-propelled particles: stabilizing symmetric formations on closed curves. *In*

Proc. 45th IEEE Conf. Decision and Control, pages 5067–5072, December 2006.

[32] D. A. Paley, N. E. Leonard, R. Sepulchre, D. Grünbaum, and J. Parrish. Oscillator models and collective motion: Spatial patterns in the dynamics of engineered and biological networks. *IEEE Control Systems Magazine, to appear August 2007.*

[33] P.M. Poulain and P.P. Niiler. Statistical analysis of the surface circulation in the california current system using satellite- tracked drifters. *Journal of Physical Oceanography*, 19:1588–1603, 1989.

[34] S. R. Ramp, R. E. Davis, N. E. Leonard, I. Shulman, Y. Chao, A. R. Robinson, J. Marsden, P. Lermusiaux, D. Fratantoni, J. D. Paduan, F. Chavez, X. S. Liang, W. Leslie, and Z. Li. The Autonomous Ocean Sampling Network (AOSN) Predictive Skill Experiment in the Monterey Bay. *Deep-Sea Research II*, submitted, 2007.

[35] D. L. Rudnick, R. E. Davis, C. C. Eriksen, D. M. Fratantoni, and M. J. Perry. Underwater gliders for ocean research. *Marine Technology Society Journal*, 38:48–59, 2004.

[36] R. Sepulchre, D. A. Paley, and N. E. Leonard. Stabilization of planar collective motion: All-to-all communication. *IEEE Transactions on Automatic Control*, 52(5), 2007.

[37] R. Sepulchre, D. A. Paley, and N. E. Leonard. Stabilization of planar collective motion with limited communication. *IEEE Transactions on Automatic Control*, to appear.

[38] S. Strogatz and I. Stewart. Coupled oscillators and biological syncronization. *Scientific American*, 269:68–74, December 1993.

[39] S. H. Strogatz. From Kuramoto to Crawford: Exploring the onset of synchronization in populations of coupled oscillators. *Physica D*, 143:1–20, 2000.

[40] M. Veneziani, A. Griffa, A. M. Reynolds, and A. J. Mariano. Oceanic turbulence and stochastic models from subsurface lagrangian data for the northwest atlantic ocean. *Journal of Physical Oceanography*, 34:1884–1906, 2004.

[41] N. Wiener. *Nonlinear Problems in Random Theory.* MIT Press,Cambridge, MA., 1958.

[42] N. Wiener. *Cybernetics, 2nd Edition.* MIT Press, Cambridge, MA, 1961.

[43] A. T. Winfree. *J. Theoret. Biol*, 16:15, 1967.